JGR Space Physics

RESEARCH ARTICLE
10.1029/2019JA027484

Investigating Magnetosphere-Ionosphere-Thermosphere (M-I-T) Coupling Occurring During the 7–8 November 2004 Superstorm

Ildiko Horvath[1] and **Brian C. Lovell**[1]

[1]School of Information Technology and Electrical Engineering, The University of Queensland, Brisbane, QLD, Australia

Key Points:
- High electron and neutral densities within/over flow channels demonstrate an apparent strong M-I-T coupling during SED events
- Low electron and high neutral densities within/over flow channels falsely suggest an apparent weak M-I-T coupling during erosion events
- Plasmaspheric erosion was due to the interaction of strong magnetospheric convection and SAPS E fields during strong M-I-T coupling

Correspondence to:
I. Horvath,
ihorvath@itee.uq.edu.au

Citation:
Horvath, I., & Lovell, B. C. (2020). Investigating magnetosphere-ionosphere-thermosphere (M-I-T) coupling occurring during the 7–8 November 2004 superstorm. *Journal of Geophysical Research: Space Physics*, *125*, e2019JA027484. https://doi.org/10.1029/2019JA027484

Received 1 OCT 2019
Accepted 4 FEB 2020
Accepted article online 7 FEB 2020

Abstract In this study, we investigate the shock-sheath driven 7–8 November 2004 superstorm for its flux transfer events and resultant flow channel (FC) events and associated neutral (D_N) and electron (Ne) density features in order to understand better the underlying coupled magnetosphere (M) and ionosphere (I) processes and responses in the thermosphere (T). We focus on the (i) subauroral, auroral, and polar cap regions, (ii) localized D_N increases and associated Ne features and FCs developed, and (iii) energy deposition occurred. Results show the development of localized D_N increases (1) within/over FCs and associated enhanced small-scale field aligned currents suggesting Joule heating driving upwelling during forward and reverse polar convections, (2) appearing with Ne increases during storm-enhanced density (SED) events suggesting strong M-I-T coupling and with Ne depletions during plasmaspheric erosion events suggesting weak M-I-T coupling, and (3) in the thermosphere's increasing NO and continuously low O/N_2 composition regions. During erosion events, strong storm-time subauroral polarization streams (SAPS) E fields developed. Meanwhile the well-developed plasmapause appeared with decreased total electron content (TEC) on its poleward side and with increased TEC and Ne (appearing as a shoulder feature that is the signature of SED) on its equatorward side. From these we conclude that although strong M-I-T coupling was apparent during SED events, M-I-T coupling was also strong during erosion events when the combination of strong convection E field and large storm-time SAPS E fields eroded the high-latitude region and thus decreased the high-latitude Ne and TEC.

1. Introduction

Magnetic reconnection is a process that facilitates the interconnection of interplanetary magnetic field (IMF) and geomagnetic field and thus allows the transfer of mass/energy/momentum from the Earth's magnetosheath to the magnetosphere (M) and then to the ionosphere (I) and thermosphere (T) creating a coupled M-I-T system. Reconnection with a time-varying nature produces a series of flux transfer events (FTEs; Russell & Elphic, 1978, 1979) characterized by a lifetime of ~10–15 min and repetition interval of ~8 min (Kuo et al., 1995; Russell et al., 1996; Sandholt et al., 1996). During FTEs, the reconnected magnetospheric flux tubes convect poleward or equatorward, perturb the local magnetic field and cause its local reversal, and thus leave their bipolar signatures behind. This bipolar signature is widely recognized as the FTEs' typical magnetospheric footprint, became a generic norm to identify FTEs, and can be tracked by the local B field component directed normal (N) to the magnetopause, called B_N, since the flux tube is naturally oriented parallel to the magnetopause (Rijnbeek et al., 1984).

As the magnetosphere couples with the ionosphere, the FTE's ionospheric signatures appear at ionospheric altitudes as (i) auroral events, (ii) plasma convections and flow channels (FCs), and (iii) large-scale field aligned currents (FACs). Regarding (i) auroral events, the dayside auroral oval is highly dependent upon the IMF's orientation and shifts equatorward ($B_Z < 0$) or poleward ($B_Z > 0$; Sandholt et al., 1983) in both hemispheres and dawnward ($B_Y > 0$) or duskward ($B_Y < 0$) in the Northern Hemisphere while opposite scenarios characterize the Southern Hemisphere (Sandholt & Farrugia, 2009). Characteristic auroral signatures observed during FTEs across the low- or high-latitude dayside magnetopause appear as type-1 aurora and poleward moving auroral forms (PMAFs; Sandholt & Newell, 1992) or type-2 aurora, respectively (Sandholt et al., 1996). These aurorae develop where their respective X line reconnection events of X_L at low latitude and X_H at high latitude occur (Sandholt & Farrugia, 2002). In terms of polar convection (ii), convection flows become pulsed during FTEs and thus appear as high-speed flows (e.g., Neudegg et al., 2000) or

FCs. These are classified as FCs 1–3 occurring during forward (Dungey, 1961) convection and as FC-4 developing during reverse (Dungey, 1963) convection (see details in Andalsvik et al., 2011). FC-1 occurs during dayside magnetopause (or X_L) reconnection, appears as an enhanced sunward auroral plasma flow, and is associated with newly open field lines. In the forward polar convection's subsequent stages, when the newly open field lines become old open (~10–20 min after reconnection; Sandholt et al., 2010), FC-2 and then FC-3 appear as enhanced polar antisunward flows and thus are associated with old-open field lines. But their respective reconnection processes occur at the dayside magnetopause (FC-2) and at the nightside magnetotail (FC-3; Sandholt & Farrugia, 2012). FC-4 is also associated with old-open field lines but appears during reverse polar convection as a cross-polar sunward flow. Thus, these FC-1–FC-4 are the ionospheric signatures of efficient energy and momentum transfer occurring on open-field lines and within FCs (Sandholt et al., 2010). In terms of M-I coupling (iii), large-scale magnetospheric FACs communicate reconnection bursts from the magnetopause (Glassmeier & Stellmacher, 1996) and electromagnetic stress from the magnetosphere to lower altitudes, and thus couple the M-I system (e.g., Farrugia et al., 2003). M-I current systems include the Region 1 (R1) and Region 2 (R2) FACs where R1 FACs flow downward/upward in the morning/evening hours and R2 FACs show an opposite polarity in any local time sector and are situated equatorward of the R1 FACs (Iijima & Potemra, 1978). FC-related convection enhancements are due to the connections of large-scale FACs via ionospheric Pedersen currents within FCs, while the prevailing low ionospheric conductivity leads to enhanced electric (E) fields that drive both Pedersen currents and FCs (Sandholt & Farrugia, 2009). A scenario like this occurs in the dusk-premidnight sector at subauroral latitudes giving rise to the development of subauroral polarization streams (SAPS; Foster & Burke, 2002) E field, according to the current generator theory (Anderson et al., 1993; Anderson et al., 2001). Accordingly, downward (↓) R2 FACs flow into the low-conductivity region of the evening midlatitude ionospheric trough, situated equatorward of the electron aurora, and connect with upward (↑) R1 FACs via poleward Pedersen currents. The resultant poleward SAPS E field drives the strong sunward SAPS FC (Anderson et al., 2001; Foster & Burke, 2002) that can exceed ~4,000 m/s and can reach ~5,000 m/s in the topside ionosphere (Anderson et al., 2001). But the connection of ↑R1-↓R2 FACs at the SAPS FC's poleward edge negates the current generator theory and implies the short circuiting of substorm injected plasma jets over the plasmapause (PP) (Mishin, 2013). According to the voltage generator theory (Southwood & Wolf, 1978), the SAPS FC can also develop when a gap forms between the inner edges of proton and electron plasma sheets and generates a poleward polarization E field in the low-conductivity evening midlatitude trough.

The dynamics of the plasmasphere are controlled by the convection E field in the magnetosphere. During magnetically active times, the enhanced convection E field erodes the plasmasphere by peeling off its outer layer (Grebowsky, 1970). But in the dusk sector, the strong SAPS E field—due to its close proximity to the PP—develops in the plasmasphere and thus plays also a major role in plasmaspheric dynamics such as plasmaspheric erosion (Puhl-Quinn et al., 2007). In a typical erosion event, the dusk-nighttime PP moves earthward and appears with a steep radial gradient (Goldstein et al., 2003). Meanwhile, the peeled off plasma appears as a broad plume of storm-enhanced densities (SEDs; Foster, 1993), also called SED plume or erosion plume, which comprises the eroding plasmasphere's outer boundary (Foster et al., 2002). But the duskside sunward convection flow on its own is not strong enough for plume formation, and thus, the dusk SAPS flow has a significant role in strengthening the sunward flow (Goldstein et al., 2003). Thus, SED plume is the signature of plasmaspheric tail drawn out by the strong convection and SAPS E fields from its dusk-time source and carried sunward to the dayside cusp by the equatorward edge of SAPS E field (Foster et al., 2002, 2004, 2007). Meanwhile, the prompt penetrating E fields (PPEFs) empower the strong forward plasma fountain leading to a well-developed equatorial ionization anomaly (EIA) with a large SED feature appearing poleward of each EIA crest (Tsurutani et al., 2004), on the equatorward side of the midlatitude trough. Thus, erosion signatures include the PP appearing in a well-developed form as depicted by its steep electron/ion density gradient and appearing often with a shoulder (i.e., SED feature) on its equatorward side (Tsurutani et al., 2004). But density decrease also occurs on the PP's poleward side due to both the SAPS E field's equatorward movement with respect to its quiet-time position (Tsurutani et al., 2004) and the thermospheric neutral composition change (Rishbeth, 1998).

Via M-I-T coupling, the transferred mass/energy/momentum to the thermosphere leads to Joule and electron heating generating storm-time equatorward directed thermospheric wind surges, which, in turn, drive both neutral gas upwellings and composition changes. These changes can be parameterized and quantified

by (i) the O/N_2 ratio of which decrease or increase causes ionospheric depletions or enhancements, respectively, and of which changes can be redistributed by horizontal neutral winds and molecular redistribution latter on (Kil et al., 2011) and by (ii) the NO content of which overproduction, caused by low-energy (<1 keV) particle precipitations, results in reduced thermospheric uplift and density increase due to cooling (Knipp et al., 2013, 2017). But these storm time thermospheric wind surges and resultant composition changes are unlikely to cause large ionospheric plasma density depletions on their own (Clilverd et al., 2000). The combination of strong convection and SAPS E fields is needed to erode the dusk sector plasmasphere (Foster et al., 2005). Therefore, in order to understand the coupled M-I-T system, it is significant to understand how the coupling occurs between the magnetosphere and ionosphere and how the thermosphere couples with the coupled M-I system.

In this study, the main focus is on M-I-T coupling occurring during the 7–8 November 2004 superstorm. We analyze how the magnetosphere coupled with the ionosphere and then to the thermosphere in order to better understand the underlying physical mechanisms. We also analyze the relations of FTEs to the localized neutral density (D_N) increases by investigating the development of these D_N increases within/over their respective FCs, since FCs are the ionospheric signatures of FTEs, and by specifying the FC types. We also investigate the development of localized D_N increases during SED events and during plasmaspheric erosion events.

2. Database and Methodology

Our multisatellite and multi-instrument database contains in situ measurements provided by the satellites of Cluster, Los Alamos National Laboratory (LANL), Polar, Challenging Minisatellite Payload (CHAMP), Thermosphere Ionosphere Mesosphere Energetics and Dynamics (TIMED), Defence Meteorological Satellite Program (DMSP), and Global Positioning System (GPS).

From the four identical Cluster (C1–C4) satellites, orbiting the Earth in 57 hr at ~90° inclination, we utilized C1 measurements in Geocentric Solar Ecliptic (GSE) coordinates. These include the FluxGate Magnetometer's (FGM; Balogh et al., 2001) B field vectors (B_X, B_Y, B_Z; nT) and total B magnitude (B_T; nT), the Hot Ion Analyser's (HIA; Rème et al., 2001) ion density (Ni; cm^{-3}) and bulk velocity components (V_X, V_Y, V_Z; km/s). Orbit data utilized include spacecraft position, invariant latitude (ILAT; °N), magnetic local time (MLT; hr), and L_Shell (R_E) values.

The LANL satellites fly on geosynchronous orbits at a radial distance of ~6.6 R_E (Birn et al., 1998). From their Magnetic Particle Analyzer (MPA) instruments, L0 and L1 provided low energy (1–130 eV/e) ion density (Ni; cm^{-3}) and velocity component (V_X, V_Y, V_Z; km/s) measurements. We smoothed the velocity data by computing their 14-min running averages.

The Polar satellite's ~80° inclined, and ~18-hr orbit has a ~2.2 R_E perigee and ~9 R_E apogee. Total plasma density (Np; cm^{-3}) and spacecraft potential ($V_{S/C}$; V) plus electron density (Ne; cm^{-3}) measurements are from the Electric Field Investigation (EFI) instrument (Harvey et al., 1995) plus Hydra Plasma Instrument (Scudder et al., 1995), respectively. The Hydra Fast Plasma Analyzer measured the mean electron energy (Ee; eV) parallel ($Ee_{||}$) and perpendicular ($Ee_{\perp}$). Orbit data employed include spacecraft position, MLT (Hr), magnetic latitude (MLAT; °N), and L_Shell (R_E)values.

The CHAMP satellite's sun-synchronous and circular ($T \approx 92$ min) orbit is dusk-dawn oriented, ~87° inclined, and situated in the ~360–400 km altitude range. Its accelerometer measurements provide neutral density (D_N; kg/m^3) values and wind speed (U_W; km/s) data that are converted to the local coordinate system's zonal east-west direction (Doornbos et al., 2010). Electron density (Ne; 10^{+3} e/cm^3) and electron temperature (Te; K) measurements are from the Planar Langmuir Probe (PLP). The raw SS-FAC values, obtained from the magnetometer data, are smoothed by computing their 16-s running averages.

The TIMED satellite circles the Earth at ~625 km altitude in a ~74° inclined orbit ($T \approx 97$ min). The Sounding of the Atmosphere using Broadband Emission Radiometry (SABER; Russell et al., 1999) instrument records the infrared radiance of various atmospheric trace species including nitric oxide (NO) at 5.3 μm. We utilized the NO emission data ($mW/m^2/sr$) recorded at 140-km altitude.

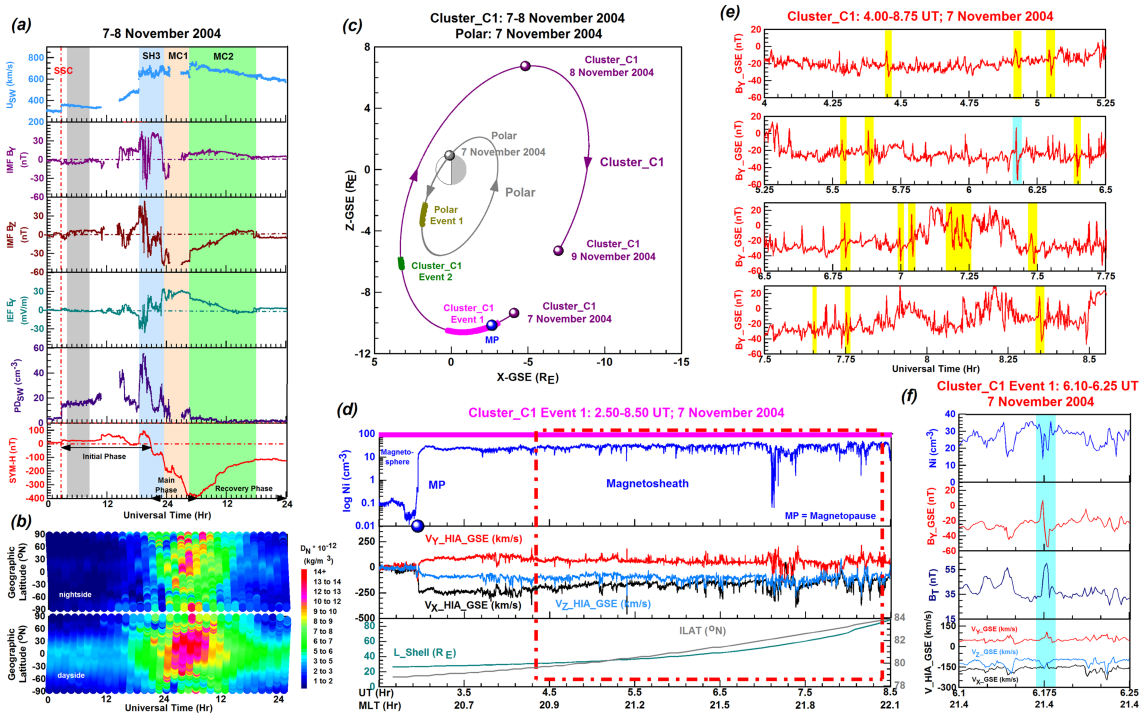

Figure 1. The evolution of 7–8 November 2004 geomagnetic superstorm is depicted (a) by a series of solar wind and interplanetary measurements and (b) by the storm impact of the nightside and dayside thermospheric neutral density (D_N). During that time, (c) Polar and Cluster_C1 detected their respective events. During Cluster_C1 Event 1, (d) C1 tracked the magnetopause (MP) and (e) a series of flux transfer event depicted by +/− B field rotations and (e) their other characteristics.

The polar orbiting DMSP F15 and F16 spacecraft circle the Earth at ~840-km altitude with an orbital period of ~101 min and inclination angle of ~98.7°. We utilized ion density (Ni; i^+/cm^3), electron and ion temperature (Te, Ti; K), cross-track ion drift (V_{HOR}, V_{VER}; m/s) values measured in the horizontal (sunward-antisunward) and vertical (upward-downward) directions, respectively, and the magnetic deflection components (δB_Y, δB_Z; nT; sunward-antisunward). By following the methodology of Huang and Burke (2004) and Huang et al. (2014), we computed the vertical component of the Poynting flux (S_{VER}; mW/m^2; sunward-earthward). But for our presentations, we show the earthward values as positive values.

GPS total electron content (TEC; TECU where 1 TECU = 10^{16} e^-/m^2) values, obtained from the Madrigal Database of Haystack Observatory and are computed for the 350 km mean ionospheric height, are utilized for tracking ionospheric responses.

For monitoring interplanetary conditions, we employed accurately time shifted (to the nose of the bow shock) solar and interplanetary magnetic field (IMF) measurements provided by the OMNI database. These include the solar wind speed (U_{SW}; km/s), proton density (PD_{SW}; cm^{-3}), the Y (east-west) and Z (north-south) components of the IMF (B_Y, B_Z; nT) in GSE coordinates, and the interplanetary electric field (IEF) E_Y component (mV/m) in geocentric solar magnetic (GSM) coordinates. Meanwhile, the SYM-H and ASY-H (nT) indices permitted monitoring ring current variations and specifying storm phases.

3. Results and Interpretations

3.1. The 7–8 November 2004 Superstorm and Cluster_C1 Event 1

Figures 1a and 1b illustrate the unfolding of 7–8 November 2004 superstorm and the thermosphere's daytime and nighttime neutral density responses. Figure 1a's line plots are constructed with solar data and the SYM-H index. These show the variations of solar wind speed (U_{SW}), IMF B_Y and B_Z components, solar wind

proton density (PD_{SW}), and IEF E_Y. As marked, the SYM-H time series depicts the storm phases. Based on the first sudden U_{SW} increase, the sudden storm commencement (SSC) occurred at ~3.0 UT on 7 November, registered the onset of a long initial phase (3.0–21.0 UT), and was followed by a series of shocks. According to previous studies (Echer et al., 2009, 2010; Tsurutani et al., 2008; Verkhoglyadova et al., 2017), these shocks occurred in the sheath (SH) and in the magnetic cloud (MC). We mark SH3 starting at ~18.5 UT on 7 November, and MC1 and MC2 beginning at ~23.28 UT on 7 November and ~4.8 UT on 8 November, respectively (shaded intervals). Before and during these shocks marked, IEF E_Y became increasingly strong, from ~10 to ~30 mV/m, implying increasingly strong magnetospheric E field, plasma convection, and plasma erosion (Grebowsky, 1970). Within the main phase (21.0–12.0 on 7–8 November), the SYM-H index remained relatively stable at ~−90 nT for a while (21.5–23.0 UT) because of the northward turning of B_Z implying both the development and the maintenance of ring current under northward B_Z conditions (Du et al., 2008). Registering the onset of recovery phase at ~5.9 UT on 8 November, SYM-H reached its minimum of ~ −394 nT during a ~16-hr southward B_Z orientation (~20.0–12.0 UT on 7–8 November). Periodic PD_{SW} enhancements, coinciding with these sudden U_{SW} increases, imply that these shocks propelled solar wind protons into the IMF and thus increased its strength (Echer et al., 2009, 2010; Tsurutani et al., 2008; Verkhoglyadova et al., 2017). In Figure 1b, the nighttime and daytime CHAMP D_N maps depict the most dramatic thermospheric neutral density increases occurring during this ~16-hr $B_Z < 0$ time period.

In Figure 1c, the X vs. Z plot in GSE coordinates illustrates the orbit sections of Cluster_C1 on 7–8 November and Polar on 7 November. Polar started its journey in the northern polar region on 7 November and its dayside southern section of our interest is marked as Polar Event 1 (dark yellow) and tracked sunward flowing drainage plumes (see Figure 9b and section 3.4). Meanwhile, C1 commenced its journey on 7 November over the Southern Hemisphere and completed almost a whole orbit by the end of 8 November. Soon after its journey started on 7 November in the magnetosphere at $L \approx 27\ R_E$, C1 crossed the magnetopause (MP; indicated as symbol dot in blue) at $L \approx 27R_E$ and continued in the magnetosheath ($L > 27\ R_E$) as the satellite moved away from the Earth. This orbit section is marked as Cluster_C1 Event 1 (magenta) and tracked a series of FTEs. The following FTEs investigated occurred during Cluster_C1 Event 2 (green).

Figure 1d depicts Cluster_C1 Event 1, during 2.5–8.5 UT on 7 November, with the time series of log Ni, Vi, L_Shell, and ILAT values. Clearly visible features shown are the MP's steep density gradient, and the regions of magnetosphere ($25.5\ R_E < L < 27\ R_E$) and magnetosheath ($27\ R_E < L < 94.6\ R_E$). These regions are characterized by their respective quiet and active ion drift conditions and by their lower and higher ion densities (e.g., Le et al., 2008; Pitout et al., 2001). As C1 moved into the magnetosheath, its orbit track covered high latitudes (79°S < ILAT<83°S) and tracked a series of high-latitude FTEs (see Figure 1e) at the beginning of long initial phase (marked as shaded interval in gray in Figure 1a) when the IMF was northward ($B_Z > 0$) directed.

Figure 1e's B_Y line plots cover the total time period of 4.0–8.6 UT within Cluster Event 1 and depict the signatures of these high-latitude FTEs (shaded intervals) appearing as a series of bipolar signatures with +/− B_Y rotations created by the motions of open flux tubes produced by their transient reconnections (Russell & Elphic, 1978). These +/− B_Y rotations imply that the flux tubes moved poleward. This is consistent with the C1 orbit track during Cluster Event 1. Then, C1 was travelling poleward and almost parallel with the X-GSE axis, while B_Y was oriented perpendicular (or normal) to this orbit path tracking the magnetopause. Because of this orbit alignment in GSE coordinates, the B_Y component was naturally oriented as a B_N component and was able to detect the FTEs' +/− bipolar signatures. Figure 1f illustrates this bipolar signature in more detail and along with other characteristics (shaded interval in cyan). These include the locally depleted plasma ion density within the flux tube plus the locally increased B_T and Vi components, which are also important bipolar signatures (e.g., Le et al., 2008).

3.2. Localized Neutral Density Increases Detected by CHAMP During FC Events

Figures 2a to 2c are constructed with a set of CHAMP and TIMED/SABER time series and cover the second half of initial phase (10.0–21.0 UT on 7 November) and almost the entire main phase (~21.0-10.3 UT on 7–8 November). CHAMP tracked localized neutral density (D_N) increases in each hemisphere's polar region when the zonal winds became pulsed as indicated by the positive and negative zonal wind speed (U_W) amplitudes. These U_W amplitudes imply a series of events, such as the development of FTEs, the development

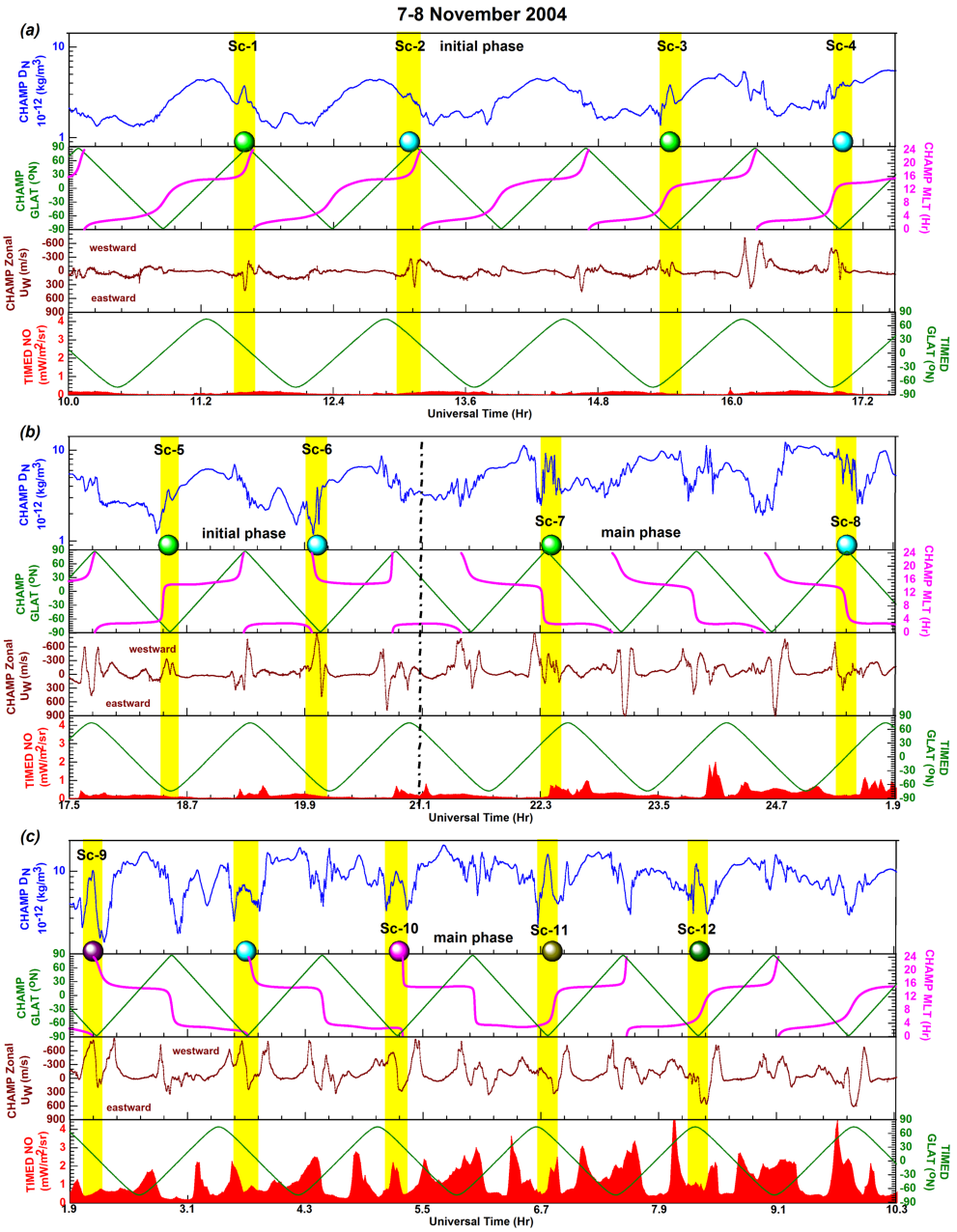

Figure 2. The time series illustrate the UT variations of CHAMP measured thermospheric neutral density (D_N), geographic latitude (GLAT), magnetic local time (MLT), and zonal wind speed (U_W) plus TIMED measured NO (nitric oxide) content and GLAT during the time period of 10.0–10.3 UT on 7–8 November 2004 when CHAMP detected as a series of localized D_N increases over the polar regions (shaded intervals in yellow) while NO content increased. Scenarios 1–12 are marked.

FCs, and the consequential development of localized neutral density increases within/above these FCs (Carlson et al., 2012). The daytime CHAMP scenarios (Sc-1–Sc-12), investigated in this study, are marked. Meanwhile, the TIMED satellite crossed the polar region at similar UTs as CHAMP, since the two satellites were nearly coplanar during this storm (Lei et al., 2010). In each hemisphere's polar region, the TIMED/SABER measured NO content at ~140 km altitude shows an increase from a low <0.5 $mW/m^2/sr$ (during the initial phase) to a high ~2–4 $mW/m^2/sr$ (during the main phase). But the increasing NO content still permitted the development of localized D_N increases (shaded intervals) and CHAMP tracked their best development in the second half of main phase (Sc-9–Sc-12).

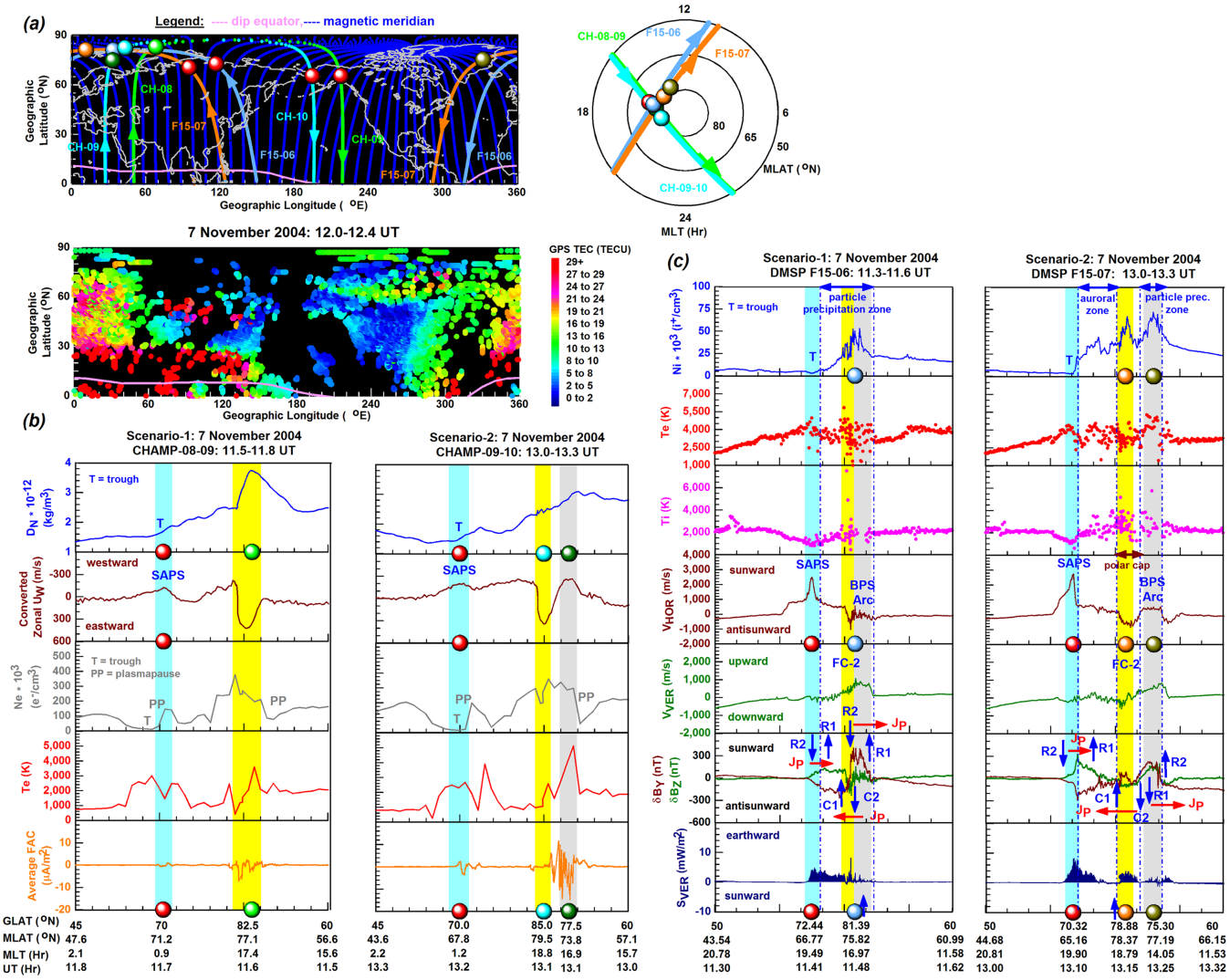

Figure 3. (a) The Northern Hemisphere map (top panel) shows the ground tracks of the CHAMP and F15 passes employed and the locations of the features of interest (colored dots) that are also shown in the MLT vs. MLAT polar plot, while the GPS TEC map (bottom panel) depicts the ionosphere. (d) The CHAMP polar cross sections are constructed with neutral density (D_N), zonal wind speed (U_W), electron density (Ne), electron temperature (Te), and averaged field aligned current (FAC) data. (c) The matching F15 polar line plot sets are constructed with ion density (Ni), electron and ion temperature (Te, Ti), cross-track ion drifts (V_{HOR}, V_{VER}) in the horizontal (HOR) and vertical (VER) directions, magnetic deflection components (δB_Y; δB_Z), and Poynting flux (S_{VER}). The vertical arrows indicate spacecraft turnings. Scenarios 1 and 2 show the localized D_N increases within/over flow channels (FC-2s) and BPS arcs and their associated storm-enhanced density (SED) features and increased Te and field aligned currents (FACs), and the well-developed subauroral polarization streams (SAPS) FCs.

3.2.1. Initial Phase Scenarios 1–4: Localized Neutral Density (D_N) Increases Developed During FTEs Within/Over FCs 1 and 2 and Auroral Arcs, and Near the SED Plume

Figure 3 and the following Figures 4–6 are constructed in the same way. Figure 3 illustrates two Northern Hemisphere scenarios (Sc-1; Sc-2) that depict the development of localized D_N peak within/over FC-2 and postnoon auroral arcs (AAs) that are the substructures of PMAFs (Southwood, 1987; Sandholt et al., 1990) during FTEs. Overall, these scenarios show commonly that the postnoon auroral arc's low precipitation-induced conductivity led to the enhancement of both its own westward E field and the nearby FC-2's eastward E field developing under sunlit conditions and during a series of FTEs facilitating X_L magnetopause reconnection events during which the localized D_N peaks developed near the SED plume. These FTEs had been ongoing and are indicated by the ongoing development of the resultant ionospheric FC signatures.

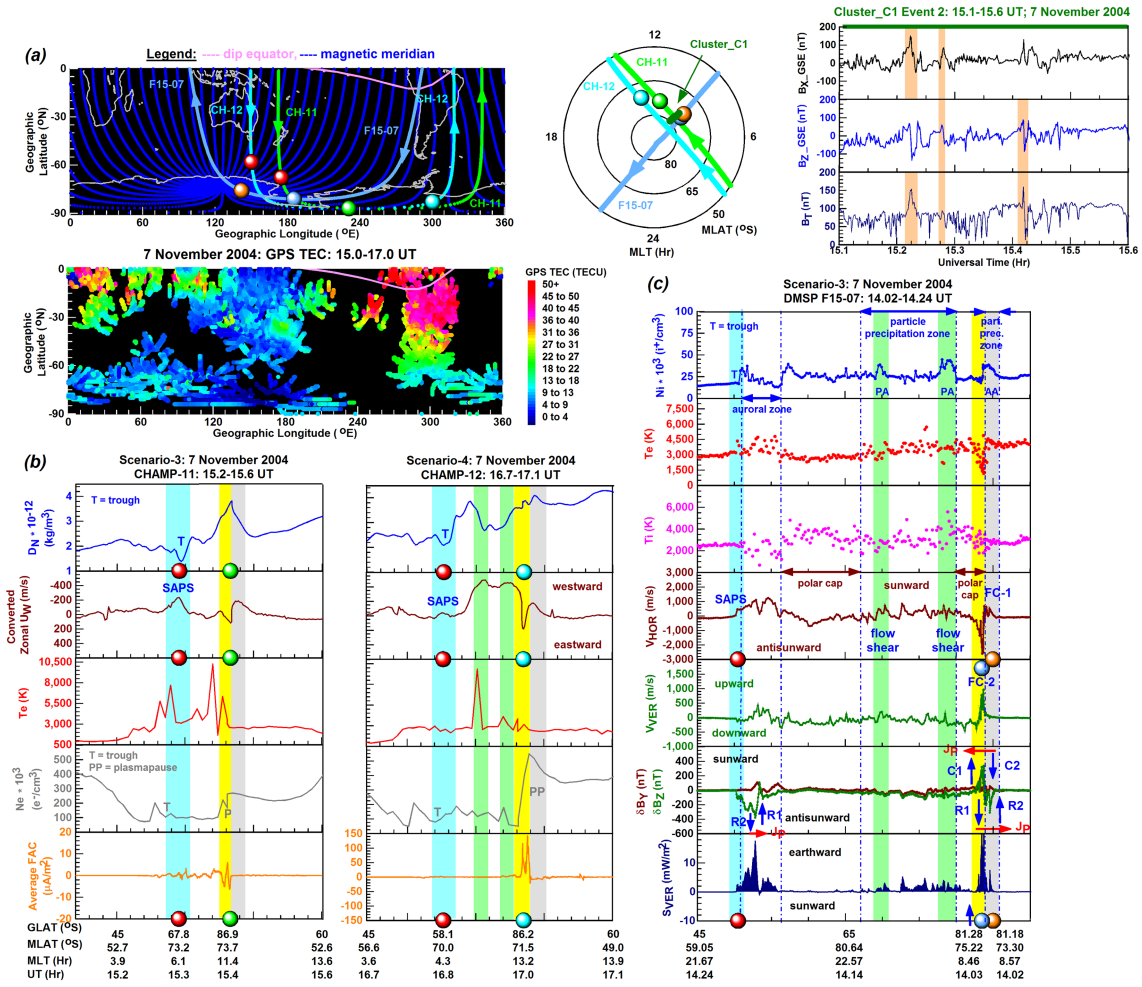

Figure 4. The same as Figure 3 but for Scenarios 3 and 4 but with the MLT vs. MLAT polar plot showing the good correlation of Cluster-C1 Event 2's FTE detections and Sc-3's FCs 1 and 2 detections and with Cluster_C1 Event-2 illustrating as series flux transfer events with the tracked +/− B field rotations and B_T increases. Scenarios 3 and 4 show the localized D_N increases within/over flow channels (FCs 1 and 2) and flow shear arcs and their associated storm-enhanced density (SED) features and increased electron temperature (Te) and field aligned currents (FACs) while the polar cap was eroded, and the well-developed subauroral polarization streams (SAPS) FCs.

Figure 3a′ Northern Hemisphere map (top panel) shows that CHAMP detected D_N increases and underlying FCs and F15 detected FCs commonly in the northern European sector and during the postnoon hours (see MLT vs. MLAT polar plot). Meanwhile the SAPS FCs (dots in red) were tracked over Alaska by CHAMP and Northern Asia by F15. As GPS TEC map (bottom panel) illustrates, the F15 detected FCs are situated at the edge of a TEC band of 8-17 TECU (shades of green) comprising the SED plume plasma's edge. The close correlation between the CHAMP and F15 detected FCs are shown with the MLT vs. MLAT polar plot.

Figure 3b shows two polar cross sections constructed, respectively, for Sc-1 and Sc-2 with multi-instrument CHAMP data. Each cross section illustrates the development of a D_N peak at polar latitudes and during a FTE and its underlying eastward FC (shaded interval in yellow), which we specify as FC-2 based on the matching F15 pass (see details below). A high-latitude D_N peak with its underlying westward FC (shaded interval in gray) was also tracked. Both Te and the averaged SS-FACs became variably enhanced within these FCs implying local downward heat flows and frictional heating (Carlson et al., 2012; Liu et al., 2010) plus Joule and particle heating (Lühr et al., 2004), respectively. These interpretations are evidenced by their correlated F15 detections (see details below). Regarding the large Ne enhancements tracked by CHAMP in each scenario, their main contributing factor was the sunward convecting high-density SED

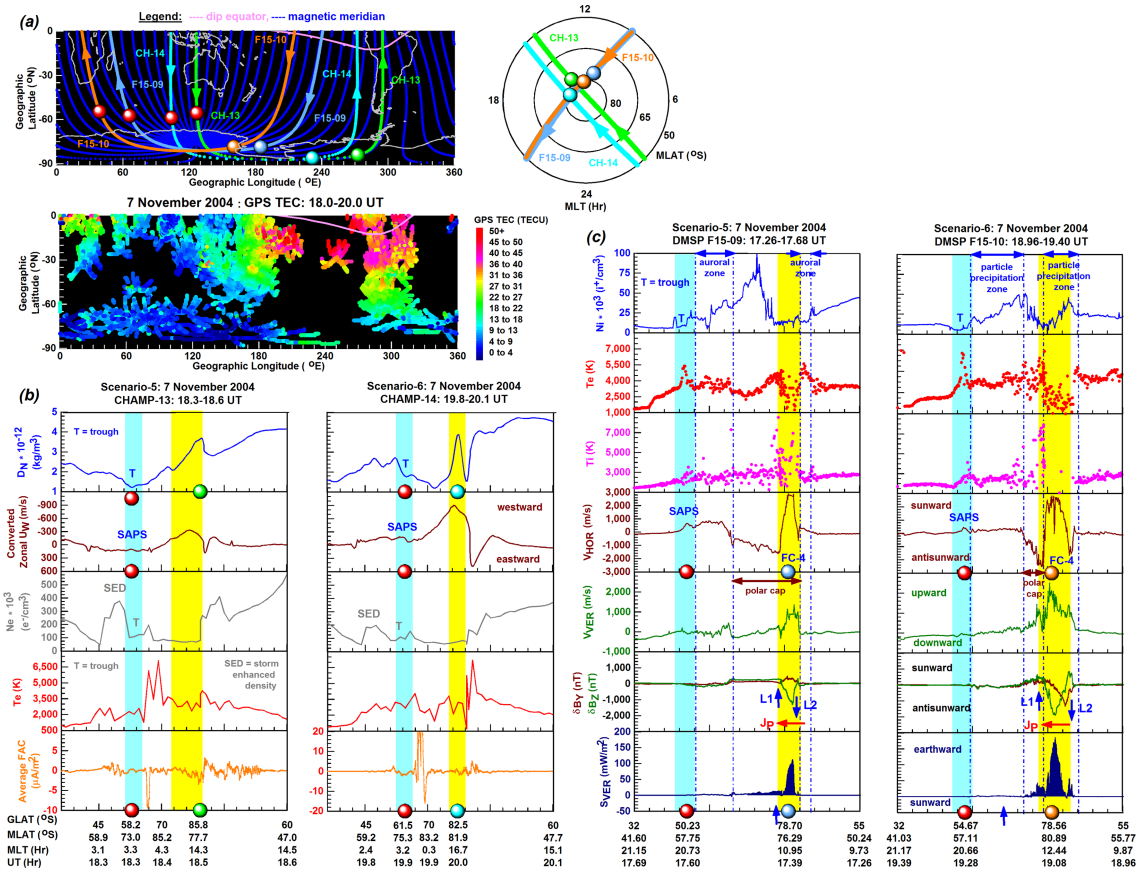

Figure 5. The same as Figure 3 but for Scenarios 5 and 6. Scenarios 5 and 6 show the localized D_N increases within/over cross-polar sunward flows (FC-4s) and their associated increased electron temperature (Te) and field aligned currents (FACs) while the polar cap was eroded and the storm-enhanced density (SED) feature appeared on the equatorward side of the trough, and some small subauroral polarization streams (SAPS) FCs.

plume plasma (see TEC map in Figure 3a) that increased also Te, due to frictional heating, as Liu et al. (2010) suggested. CHAMP tracked other features such as a well-developed SAPS FC (shaded interval in cyan) and the midlatitude trough (marked as T) that is well indicated by its low D_N and Ne and locally enhanced Te, marking the location of PP (Titheridge, 1976), at the trough minimum.

Figure 3c shows the correlated multi-instrument F15 polar line plot sets where the V_{HOR} line plots tracked under sunlit conditions two FC-2s (shaded intervals in yellow) and two westward FCs (shaded intervals in gray) with their respective BPS AAs (see also Figures 7a and 7b). These AAs are characterized by their locally enhanced Ti (~4,000 K), V_{VER} (~800 m/s), and Ni (~50–70 × 10^{+3} i^+/cm^3), which are attributed to their respective locally increased Joule heating, upwelling, and resultant locally increased ion density. These observations verify the above described local downward heat flows (Carlson et al., 2012; Liu et al., 2010) and Joule heating (Lühr et al., 2004). The westward FC's suppressed ion drifts (shaded intervals in gray) are regarded the BPS type postnoon arcs' typical signatures (Sandholt & Farrugia, 2009). Each δB_Y and δB_Z line plot shows the following. Oppositely directed R1-R2 FACs connected via equatorward Pedersen currents within these BPS type AAs where their respective resultant westward E fields drove the plasma sunward. Within each FC-2, oppositely directed cusp (C) currents (C1–C2 FACs) connected via poleward Pedersen currents driving an eastward E field and the plasma antisunward. Importantly, these eastward E fields within their respective FC-2s were boosted by the BPS arcs' low precipitation-induced conductivity (Marklund, 1984) and thus compensated for the sunlit conditions (Sandholt & Farrugia, 2009). Each V_{HOR} line plot tracked also a SAPS FC (~−2,600 and ~−2,800 m/s) where the downward ↓R2 FACs increased but the oppositely directed ↑R1–↓R2 FACs connected via poleward directed Pedersen currents at the edge of the SAPS FC implying a short-circuited system operating as a current generator (Mishin,

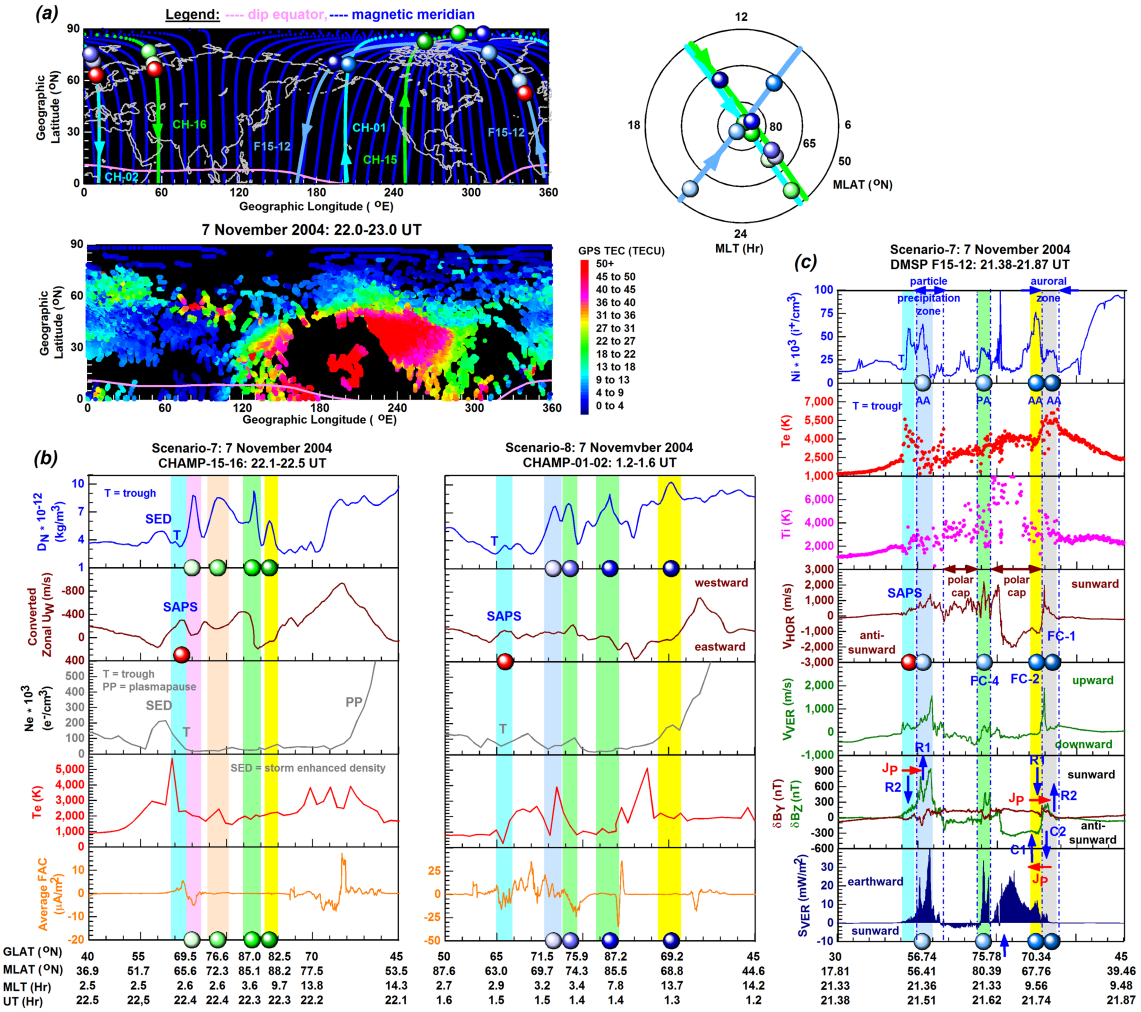

Figure 6. The same as Figure 3 but for Scenarios 7 and 8. Scenarios 7 and 8 show the localized D_N increases within/over flow channels (FCs 1 and 2 and FC-4), and their associated low electron temperature (Te) and field aligned currents (FACs) during the local nighttime hours while the polar cap became eroded and the storm-enhanced density (SED) feature appeared on the equatorward side of the trough, and subauroral polarization streams (SAPS) FCs. These FCs 1 and 2 and FC-4 were associated with auroral arcs (AAs) and polar arcs (PAs), respectively.

2013). The associated SAPS E field drove the SED plume plasma (see TEC map) sunward (Foster et al., 2005). Within the SAPS FCs, Te maximized and Ti minimized locally. As the S_{VER} plots show, electromagnetic energy became deposited earthward within the SAPS FCs (~5 mW/m^2 and ~8 mW/m^2), FC-2s (~8 mW/m^2 and ~4 mW/m^2), and BPS arcs (~2 mW/m^2).

Figure 4 illustrates two Southern Hemisphere scenarios (Sc-3; Sc-4) when the localized near noon D_N peaks developed at the SED plume plasma's edge, within/above FC-1 and FC-2 while polar cap arcs (PAs) developed in the polar cap region. Overall, these scenarios demonstrate that the dayside magnetopause X_L (associated with FCs 1 and 2) and X_H (associated with PAs) reconnection events occurring during a series of FTEs led to the development of these D_N increases at the edge of SED plume plasma, driven by the large storm-time SAPS E field (Foster et al., 2007), where their electron densities increased. But the following plasmaspheric erosions depleted the polar cap away from the SED features. The large storm-time SAPS FC reaching 5,000 m/s and occurring during Sc-3–Sc-4 was tracked by F16 over the Northern Hemisphere (see first two SAPS features in Figure 9b and details in sections 3.3–3.4).

Figure 4a's map (top panel) shows that CHAMP detected these southern D_N increases at polar latitudes in the American longitude sector. Although Southern Hemisphere TEC coverage at high latitudes and over

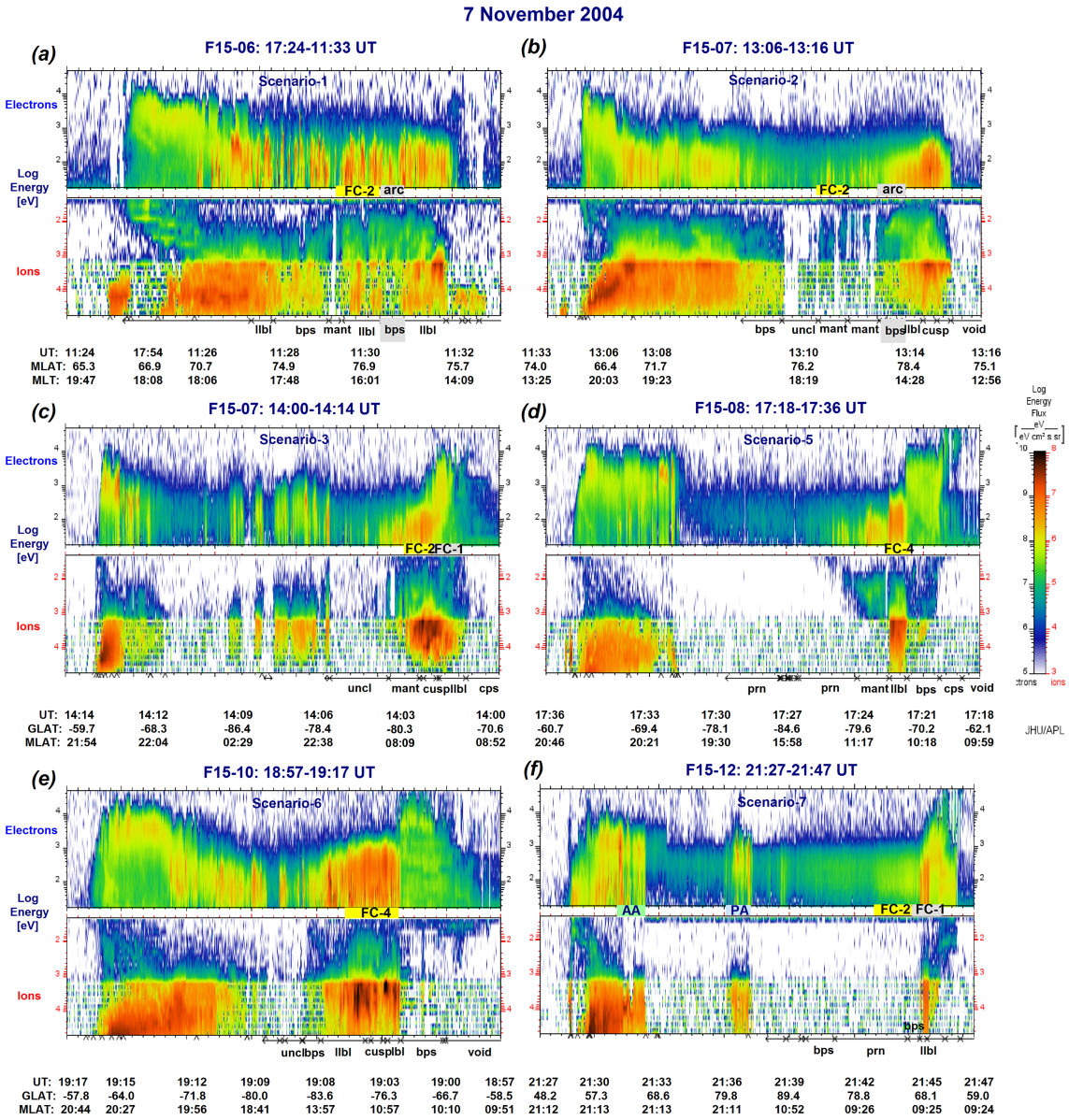

Figure 7. Spectrogram images constructed for Scenarios 1–3 and 5–7 illustrate the particle precipitation regimes of the flow channels (FCs) and arcs detected by F15.

the oceans is largely incomplete, the TEC map (bottom panel) is still able to illustrate that TEC was higher (13–18 TECU; cyan) where CHAMP detected the two near noon D_N increases (see MLT vs. MLAT polar plots). Demonstrating plasmaspheric erosion, TEC reached minimum values (0–13 TECU; shades of dark blue) at polar latitudes in the longitude sector situated between the SAPS FCs and FC-2s detected by both CHAMP and F15. According to Cluster_C1 Event 2 (15.10-15.60 UT) occurring during Sc-3, a series of FTEs occurred as indicated by the C1 measured B_X and/or B_Z magnetic field components' +/− bipolar variations and associated B_T intensifications (shaded intervals). Meanwhile, the MLT vs. MLAT polar map illustrates the close correlation of the Cluster detected FTEs and the F15 detected ionospheric signatures (FC-1 and FC-2; see details below). In Figure 4b, the two sets of CHAMP polar cross sections show that each localized D_N peak appeared with its underlying polar eastward FC (shaded interval in yellow) and auroral westward FC (shaded interval in gray). In Sc-4, CHAMP tracked also cross-polar westward drifts (shaded intervals in green). Based on the matching F15-07 pass (see details below), we specify these

CHAMP-detected FCs and westward drifts as antisunward FC-2 and sunward FC-1 and as cross-polar sunward flow shears underlying the PAs. Further CHAMP detections show that Te increased moderately within FC-2, possibly due to soft particle precipitations (Sadler et al., 2012), while the averaged SS-FACs became enhanced dramatically implying energy deposition and Joule heating (Lühr et al., 2004). Within each of these dayside D_N increases, Ne increased locally (possibly due to the SED plume plasma; see GPS TEC map) on the equatorward side of a steep Ne gradient (i.e., PP signature). While these Ne increases are attributed to the SED plume plasma, the poleward low Ne was resulted from plasmaspheric erosion driven by the strong SAPS E field (detected by F16 over the northern hemisphere; see first two plots of Figure 9c). In Figure 4c, the matching F15 line plot series tracked a similar polar cross section with a series of localized Ni increases and their underlying FC-2 (shaded interval in yellow), FC-1 (shaded interval in gray), and cross-polar sunward convections with enhanced flow shears (shaded intervals in green). These Ni increases are associated with an AA appearing in LLBL and cups precipitations (also called type-1 aurora; Sandholt & Farrugia, 2002; see also Figure 7c) and appeared within/over FC-1 on the morning side and with PAs related to the enhanced flow shears and appearing on the poleward side of weak polar rain or precipitation void (see Figure 7c). Meanwhile, the V_{HOR} line plot tracked a small SAPS FC (~1,000 m/s) wherein ↓R2 FACs increased but ↑R1–↓R2 FACs connected via poleward directed Pedersen currents outside the SAPS FC implying the operation of a short-circuited system acting as a current generator (Mishin, 2013), broad sunward polar flows with intensified flow shears underlying the PAs, a strong FC-2 (~−3,000 m/s) where oppositely directed cusp currents (C1–C2 FACs) connected via poleward Pedersen currents, and a strong FC-1 (~700 m/s) where oppositely directed R1–R2 FACs connected via equatorward Pedersen currents. These FC-1 and FC-2 detections imply ongoing FTEs and X_L magnetopause reconnection events under $B_Z \approx 0$ conditions (Sandholt & Farrugia, 2009). The close correlation between the Cluster-detected ongoing FTEs and the F15-detected FCs (i.e., ionospheric signatures of FTEs) is illustrated in Figure 4a's polar plot showing also that CHAMP passed the paths of these FCs. Meanwhile, the PAs and associated sunward flow shears are related to X_H magnetopause reconnection occurring during B_Y domination ($|B_Y|/|B_Z| \geq 1$) away from the subsolar point (Sandholt & Farrugia, 2006). According to the S_{VER} line plot, earthward energy deposition occurred within the SAPS FC moderately (~4 mW/m^2) and maximized within FC-1 and FC-2 (~20 mW/m^2) during the ongoing FTEs. Since PAs are flow shear arcs, the associated FAC intensities were small, as usual (Sandholt et al., 2004), and the underlying earthward energy deposition (~3 mW/m^2) was small.

3.2.2. Initial Phase Scenarios 5 and 6: Localized Neutral Density (D_N) Peaks Developed During FTEs and Within/Over FC-4s and Polar Arcs, and in the Eroded Polar Cap

Figure 5 illustrates two Southern Hemisphere scenarios (Sc-5 and Sc-6) when the CHAMP detected localized D_N increases developed within/above FC-4 at the polar cap's edge, in the lobe cell's LLBL or cusp precipitation regime. Overall, these scenarios demonstrate localized D_N development during the ongoing dayside X_H magnetopause reconnection and in the eroded polar cap. While there are no Cluster-detected FTE observations of these ongoing X_H reconnection events, both CHAMP and F15 detected their ionospheric signatures (i.e., FC-4s).

As Figure 5a's Southern Hemisphere maps illustrate, CHAMP detected some well-developed localized D_N increases in the American longitude sector (see top map), poleward of a medium high TEC range region (see bottom map; 13–27 TEC; shades of green) and in the midday MLT sector (see polar plot). As the storm-time SAPS E field driven plasmaspheric erosion continued (F16 detected a series of large SAPS FCs over the Northern Hemisphere during Sc-5 and Sc-6, see third and fourth plots in Figure 9c), TEC minimized (0–13 TECU; shades of dark blue) in the Australian longitude sector's high latitude region where CHAMP tracked polar latitudes. Figure 5b's CHAMP scenarios show that CHAMP tracked in the low Ne region, depicting plasmaspheric erosion, both the localized D_N increases and their underlying westward FCs that we specify as FC-4 based on the correlated F15 observations. But in these low Ne regions, electron densities further decreased within these FC-4s implying localized ion outflows (Prolss, 2006; Sadler et al., 2012) that—by acting as a driving mechanism and thus generating upwellings and localized D_N increases—could also contribute to Ne depletion (Liu et al., 2010). As lobe reconnection was unfolding within these FC-4s, the averaged SS-FACs and Te locally increased within these FC-4s implying energy deposition and local heating, respectively (as evidenced by the correlated F15 detections; see details below). While the signatures of SAPS FC can be seen in the zonal U_W data (shaded interval in cyan), the midlatitude trough and SED feature on its equatorward side were tracked by the D_N and Ne line plots, respectively. In Figure 5c, each matching F15

line plot sets depict the enhanced cross-polar sunward flows (~3,000 m/s) of FC-4, wherein oppositely directed lobe currents (L1-L2 FACs) connected via poleward directed Pedersen currents. We mention here the minimized Ni (~10 × 10^3 i^+/cm^3) within each FC-4. These Ni depletions suggest localized upwellings/outflows along with the locally maximized upward drifts (~1,000 m/s and 2,000 m/s). But the enhanced cross-polar sunward flows (~3,000 m/s) of FC-4 could also contribute to the removal of ion density by advection (Vlasov et al., 2003). Large amounts of electromagnetic energy (~100 mW/m^2 and ~180 mW/m^2 in their respective precipitation regimes of LLBL and cusp; see Figures 7d and 7e) became deposited earthward during these lobe reconnection events and within these FC-4s. Meanwhile, Ti locally increased (~8,000) implying Joule heating but Te locally minimized (~1,500 K). As the SED plume plasma became swept from the duskside to the ionospheric dayside cusp and to the magnetospheric dayside merging region and MP by the storm-time SAPS E field (see third plot in Figure 9b), the magnetosphere became preconditioned (Foster et al., 2005) and thus produced these large Poynting flux values (>100 mW/m^2). Clearly, the magnetospheric dayside merging region became a preferential dayside energy deposition site (Knipp et al., 2011).

3.2.3. Main Phase Scenarios 7 and 8: Localized Neutral Density (D_N) Peaks Developed During FTEs and Within/Over FCs and in the Eroded Polar Cap

Figure 6 illustrates two Northern Hemisphere scenarios with high-latitude localized D_N increases and their underlying eroded electron densities. Overall, these scenarios demonstrate that the development of these localized D_N increases were associated with AAs related to PMAFs and FC-2 implying dayside X_L magnetopause reconnection and forward polar convection (at $B_Z \approx 0$) and with PAs and FC-4 implying X_H magnetopause reconnection and reverse polar convection (at$|B_Y|/|B_Z| \geq 1$), while the thermospheric Ne became eroded within the polar cap by the strong SAPS E fields.

As Figure 6a's top map shows, CHAMP tracked these localized D_N increases at northern high latitudes near the end of the main phase under $B_Z \approx 0$ and$|B_Y|/|B_Z| \geq 1$ conditions and during plasmaspheric erosion events producing minimum TECs (see bottom map; 0–13 TECU; shades of dark blue) at high (60°N–90°N) geographic latitudes in the American longitude sector's larger region. These localized D_N increases propagated through the polar cap from the dayside to the nightside (see polar map). In Figure 6b, the D_N line plot tracked a series of increases of which development was associated with duskside AAs (shaded intervals in light blue), PAs (shaded intervals in green), and polar FC-2s (shaded intervals in yellow), all creating localized heating and upwelling. Meanwhile, the averaged SS-FACs became enhanced within the AAs' underlying westward FCs (shaded intervals in magenta and light blue) and also within the SAPS FC appearing in the trough region (shaded interval in cyan). Commonly, the SAPS E field led to the enhancement of Ne (i.e., SED feature) on the trough's equatorward side and to the depletion of Ne at polar latitudes demonstrating plasmaspheric erosion. Further evidence is provided by F16 detecting large SAPS E field just prior to Sc-7 (see last plot in Figure 9b). Although the development of PAs and FC-2s commonly triggered localized upwelling and Joule heating leading to the development of their respective localized D_N increases, their underlying averaged SS-FACs remained weak in the low Ne regions. Figure 6c illustrates the matching F15 polar cross sections correlated with the earlier CHAMP Sc-7. As the marked auroral zones and polar cap region illustrate, the PA (appearing at the center of polar cap filled with polar rain; see also Figure 7f) divided the polar cap into postnoon and prenoon sectors where sunward and antisunward polar convections prevailed, respectively. This can be explained with the $B_Z \approx 0$ conditions during which X_L reconnection was unfolding. Evidence is provided by FC-1 accommodating the connections of R1–R2 FACs via equatorward Pedersen currents and appearing in LLBL precipitation and by FC-2 wherein cusp (C1–C2 FACs) currents connected via poleward Pedersen currents and appearing in polar rain and in the antisunward polar convection zone. Simultaneously with the X_L reconnection and due to the$|B_Y|/|B_Z| \geq 1$ conditions, X_H or lobe reconnection was also unfolding, as implied by FC-4 with its Ni/precipitation signature specified as PA (Sandholt & Farrugia, 2006). Although F15 detected a weak SAPS FC (~400 m/s), wherein ↓R2 FACs increased and ↑R1–↓R2 FACs connected outside the SAPS FC implying a short-circuited system acting as a current generator (Mishin, 2013), the storm-time SAPS FC appeared quite large at around this time (see fourth plot in Figure 9b). Except the SAPS FC appearing in the trough region, all the other FC types detected were associated with the localized enhancements of Ni, Ti, upward drift, and strong earthward electromagnetic energy depositions reaching a maximum of ~40 mW/m^2 within the duskside AA.

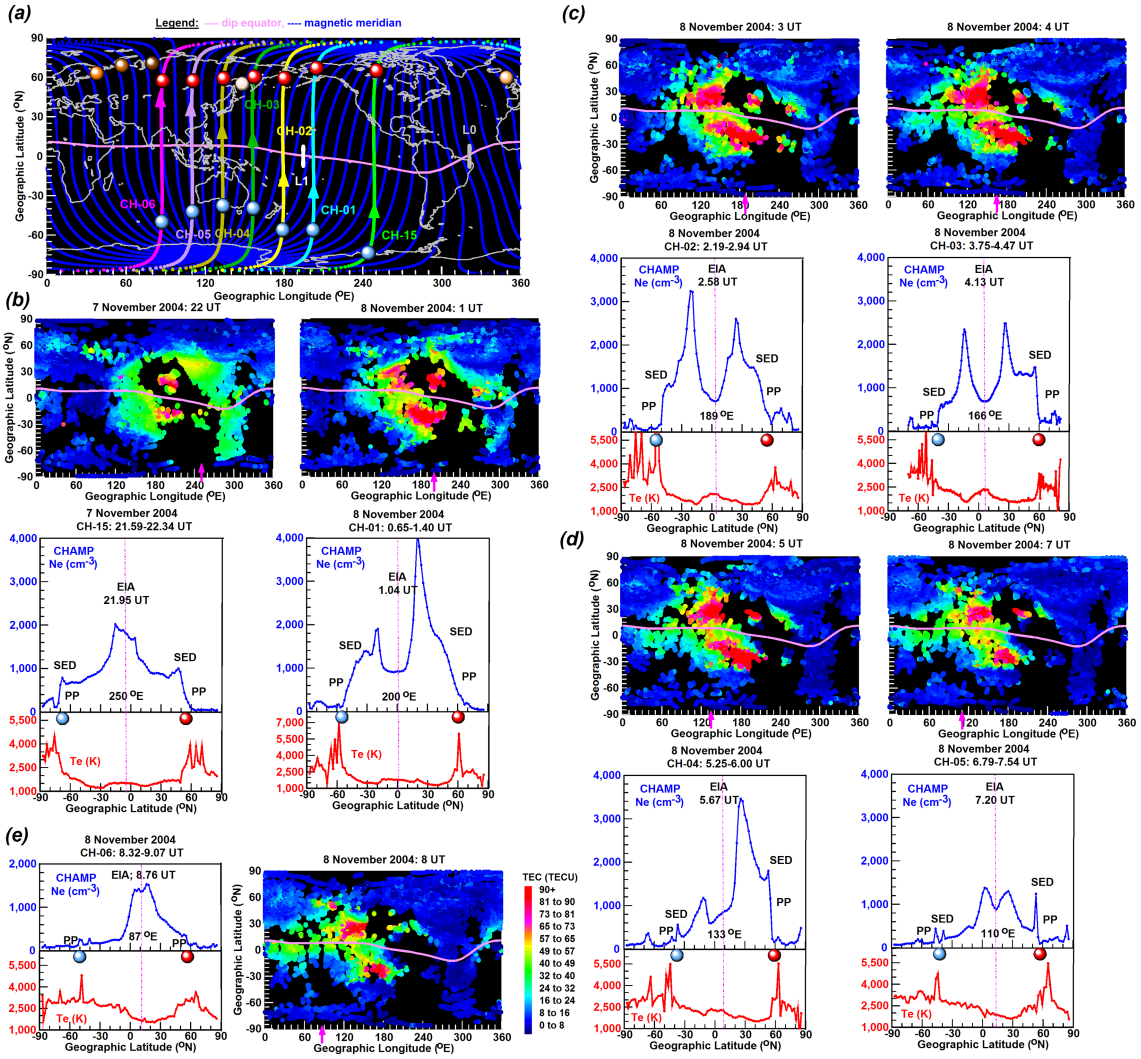

Figure 8. (a) The global map shows the ground tracks of the daytime CHAMP passes of interest, the plasmapause (PP) locations (red and blue) tracked by the CHAMP Ne line plots, the SAPS locations tracked by DMSP F16 (shaded of orange) and localized D_N increases (dots in dark magenta, yellow and green, and magenta) detected by CHAMP in the southern polar region during Scenarios 9–12. (b–e) In each set, the GPS TEC map shows in the daytime sector the well-developed equatorial ionization anomaly (EIA), the storm-enhanced density (SED) features poleward of the EIA peaks, and the eroded high-latitude regions. The arrow in magenta indicates the pole-to-pole line plot's longitude. These pole-to-pole line plots illustrate the EIA with the shoulder feature (i.e., SED feature and plasmapause [PP] appearing as a drop off), and the eroded high-latitude region poleward of the PP. The location of PP is marked by maximized electron temperatures (Te).

3.3. Plasmaspheric Erosion

Figure 8 is constructed with a series of GPS TEC maps and matching CHAMP Ne and Te line plots. Overall, these observations show plasmaspheric erosion events occurring in the longitude sector of the dayside EIA during the main phase's second half and driven by the combination of strong convection and large storm-time SAPS E fields. Large SAPS FCs had been present since the initial phase during which Sc-3–Sc-6 occurred.

Figure 8a's global map shows the ground tracks of the daytime CHAMP passes employed (CH-15 on 7 November and CH-01–CH-06 on 8 November) and the PP locations in the north (dots in red) and south (dots in blue) tracked by the CHAMP Ne line plots. We mapped also the large SAPS FCs were detected by F16 over the Northern Hemisphere (dots in shades of orange) and the localized D_N increases (dots in dark magenta, magenta, dark yellow, dark green) developed in the southern polar region (Sc-9–Sc-12) during the SAPS driven plasmaspheric erosion events. We show also the ground tracks of LANL_L0 (gray) and L1 (white) satellites crossing the magnetic equator over the Atlantic and Pacific Oceans, respectively.

Figures 8b to 8e cover the overall time period of 21.59–9.07 UT on 7–8 November situated within the 16-hr $B_Z < 0$ time period of main and recovery phases when the most dramatic thermospheric responses occurred (see details in section 3.1). Figures 8b to 8e show a series of GPS TEC and CHAMP observations made for each of the daytime CHAMP pass mapped in Figure 8a. Each observation series includes a GPS TEC map covering a 1-hr time interval of the pole-to-pole daytime CHAMP pass that provides pole-to-pole Ne and Te latitudinal cross sections. In each GPS TEC map, the arrow in magenta indicates the equatorward crossing longitude of its related dayside CHAMP pass. Except the first set where the CHAMP Ne line plot tracked an equatorial peak, these sets show (1) the EIA's two-peak structure, (2) the PP's steep Ni gradient where Te maximized, (3) the SED plume plasma appearing as a shoulder feature equatorward of the PP, and (4) the low Ne appearing poleward of the PP and thus demonstrating plasmaspheric erosion. These are further illustrated with the GPS TEC maps depicting the well-developed EIA crests (shades of red: 65-90 TECU) with the SED plume plasma on their poleward sides (shades of green; 32–57 TECU) and the eroded plasma poleward of the SED plume plasma (shades of dark blue; 0–16 TECU). These observations demonstrate that as the polar convection became enhanced, it moved the corotation/convection boundary inward or equatorward and caused with the strong SAPS E field the erosion of the midlatitude ionosphere and outer plasmasphere. Thus, both the SED feature and the steep PP gradient provide observational evidence of plasmaspheric erosion driven by the combination of strong magnetospheric convection E field and strong storm-time SAPS E field (Foster et al., 2002, 2005, 2004). Furthermore, these observations demonstrate also that the enhanced plasma fountain effects, driven by the strong PPEF and producing the well-developed EIA, also contributed to the redistribution of low latitude and midlatitude ionospheric plasma density and thus provided additional source plasma to the SED plume (Coster et al., 2007; Foster et al., 2005).

3.4. Plasmaspheric Drainage Plume

Figure 9a is constructed with LANL L0 and L1 data covering the hours of plasmaspheric erosion. The line plots of MPA low energy (1–130 eV/e) protons (Ni) tracked a series of well-developed cold (1–100 eV) SED plume plasma, while the line plots of drift velocity components (V_X, V_Y, V_Z) tracked their sunward surge in the midday (shaded intervals in magenta) and dusk (shaded intervals in blue) sectors. Their steep well-defined Ni gradients detected are the signature of plasmaspheric erosion forming drainage plumes that are driven by the strong storm-time SAPS E fields (Goldstein et al., 2004). The large SAPS FCs are shown in Figure 9b with a series of northern polar cross sections. These cover the initial phase's second half (first three sets) and the main phase's beginning (fourth set) on 7 November, and a short time period of the recovery phase (last set) on 8 November. These F16 plots illustrate large SAPS FCs, reaching ~5,500 m/s in the sunward zonal drifts (shaded intervals), just prior to the erosion events shown in Figure 8b and during the erosion events shown in Sc-3–Sc-6. The poleward edge of each SAPS FCs appeared in the close vicinity of the PP implying that these SAPS FCs developed in the plasmasphere and thus their respective SAPS E fields participated in plasmaspheric erosion (Puhl-Quinn et al., 2007). ↑R1–↓R2 FACs connected via poleward Pedersen currents at the edge of each SAPS FC (first three sets) implying a short-circuiting system acting as a current generator. Each SAPS FC received electromagnetic energy deposited earthward that reached ~180 mW/m^2 (see third set).

Figure 9c illustrates Polar_Event 1 (see also Figure 1c) unfolding during 19.3–19.8 UT on 7 November and at ~10–11 MLT. Polar crossed the PP at 19.44 UT and $L \approx 15$ (shaded interval in cyan) and MP at 19.7 UT and $L \approx 32$ (shaded interval in blue). Between them, Polar tracked the cold and dense plasmaspheric plasma of drainage plume surges (shaded intervals in magenta), as the significantly different EFI_Np and Hydra_Ne values provide evidence (Kim et al., 2007). Both the EFI_Np and the potential line plots tracked irregular peaks depicting surges of the drainage plume (shaded intervals in magenta) that are quite similar to those tracked by the LANL satellites (shaded intervals in magenta in Figure 9a). Both the $Ee_{||}$and the $Ee_{\perp}$ line plots illustrate the decreasing (from ~200 eV) and low (~40 eV) energies of these plasma surges and thus provide evidence that the dense and cold plasmaspheric plasma of the drainage plume was detected.

In Figure 9d, the time series illustrate the variations of the IMF B_Z component, SYM-H and ASY-H indices, and TIMED/SABER measured NO content. Here we marked the SAPS FC detections made by F16, the localized D_N peak detections in Sc-9–Sc-12 during the plasmaspheric erosions (shaded intervals and colored dots), and the storm time periods of SH3, MC1, and MC2 (shaded intervals). As shown, these large SAPS FCs occurred when B_Z turned southward facilitating solar wind energy input (Tsurutani et al., 1988) and

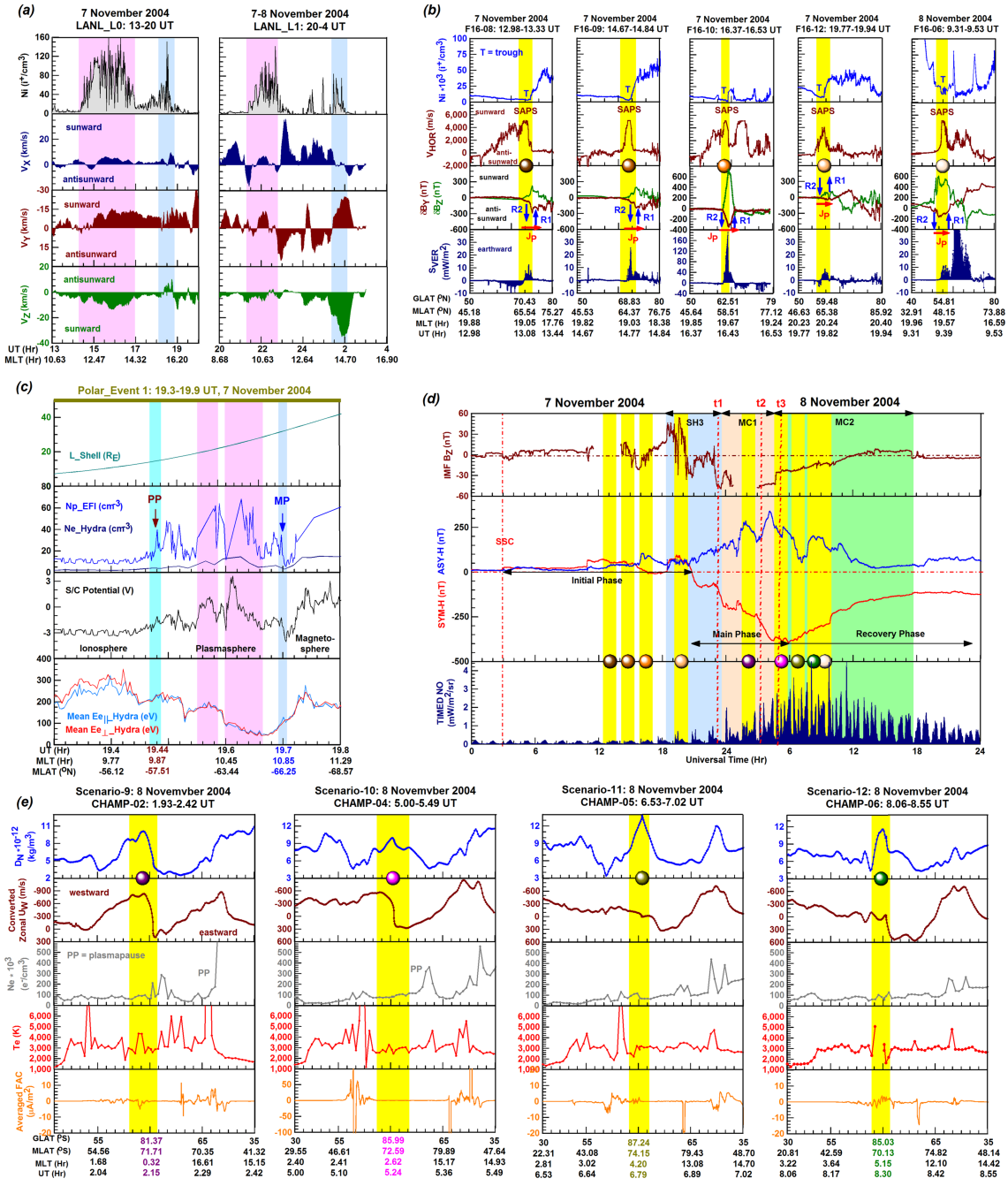

Figure 9. (a) The LANL L0 and L1 plots illustrate the sunward surging SED plume plasma. (b) The F16 line plot sets depict the SAPS FCs and earthward electromagnetic energy depositions. (c) The line plots of Polar_Event-1 tracked sunward surging cold SED plume plasma extending from the plasmapause (PP) to the magnetopause (MP). (d) The IMF B_Z, SYM-H, and ASY-H, and TIMED/SABER NO line plots illustrates that the SAPS E field (dots in shades of orange) became strong and the large localized D_N increases developed when the ring current became strongly asymmetric and while the NO content increased. (e) The CHAMP polar cross sections depict these large localized D_N increases in the eroded polar region.

the ASY-H index temporarily intensified. These simultaneous occurrences can be explained with the shock/sheath-led nature of this storm producing a strong asymmetry in the ring current (Knipp et al., 2017 and references therein) and with the asymmetric ring current-ionosphere coupling via large-scale FACs triggering and enhancing the development of SAPS FCs and thus contributing to the development of SED plume (Goldstein et al., 2003; Goldstein et al., 2004; Mishin et al., 2003) and drainage plume

extending radially outward from the greatly eroded duskside PP to the near noon MP (Foster et al., 2002, 2004). According to the 7–8 November 2004 storm study of Fejer et al. (2007), these ASY-H variations were also closely related to the PPEF's variations in the eastward and westward directions over the dip equator during the time period of 12.0–4.0 UT on 7–8 November. These eastward PPEFs drove the strong forward fountain underlying the EIA detected by CHAMP (see Figures 8b to 8e). Here, we highlight the close relation of equatorial PPEF (shown in figure 2 of Fejer et al., 2007) plus ASY-H and SAPS E field (shown in this study) —via their common driver that is the solar wind—during the plasmaspheric erosion events (21–7 UT on 7–8 November) driven by these strong storm-time SAPS E fields. Then, the TIMED/SABER measured NO content was minimal (on 7 November during SH3) and started increasing (on 8 November during MC1) and reached first its maximum (~3 $mW/m^2/sr$ during MC2). These indicate that the plasmaspheric erosion detected by CHAMP and GPS was not affected by the cooling effect of NO (see details in section 4).

In Figure 9e, the CHAMP polar cross sections illustrate Sc-9–Sc-12 when some large localized D_N increases developed within/over FCs (shaded intervals) due to the local upwelling fueled by Joule heating as the locally increased Te and averaged FACs imply, and within the eroded polar cap as demonstrated with the low Ne values.

4. Analysis of Low O/N_2, Increasing NO, and Plasmaspheric Erosion

Recent studies, investigating I-T effects during this 7–8 November 2004 superstorm, analyze the role of O/N_2 ratio in depleting or enhancing ionospheric TEC. For example, Verkhoglyadova et al. (2017) investigated directly driven I-T responses occurring promptly after a change in solar conditions and thus investigated M-I-T coupling directly driven by the solar wind. Their main events are marked as t1, t2, and t3 in Figure 9d. According to their results, the depletion of O/N_2 ratio started during SH3 causing the SYM-H to decrease to and stagnate at ~80 nT during 21.5–23.0 UT and by t1. According to our results shown in Figures 8 and 9, 21.5–23.0 UT is the time interval when CHAMP started detecting in each hemisphere plasmaspheric erosion poleward of the PP as indicated by the well-defined PP signature (i.e., Ne drop of ~1,000 cm^{-3}) and the shoulder feature (created by the SED plume plasma; Tsurutani et al., 2004) on the PP's equatorward side (see left panel of Figure 8b). Furthermore, the low O/N_2 continued between t2 and t3 during which M-I coupling maximized and a broad area of increased TEC (that we specify as SED) developed poleward of the EIA (Verkhoglyadova et al., 2017). In good agreement with their results, our results show (see Figures 8b to 8e) that CHAMP detected between t2 and t3 the well-developed EIA with this SED feature and the better developed PP signature (i.e., Ne drop of ~2,000 cm^{-3}). All these observational results described here provide evidence that the strong storm-time SAPS E field driven plasmaspheric erosion had a more significant role in depleting the high-latitude Ne and TEC, poleward of the PP, than the chemical makeup of low O/N_2 and increasing NO. The reason is the strong solar-wind driven convection E field, which is the ultimate driver of the SAPS E field since the SAPS related R1 FACs are drawn from the interplanetary generator (Foster & Burke, 2002).

5. Discussions

Our Scenarios 1–4 demonstrate strong M-I-T coupling when the localized neutral density (D_N) enhancements developed during (i) FTEs unfolding as X_L reconnection and (ii) within/over FC-1 and FC-2 associated with AAs such as BPS arcs or PMAFs, while the storm-time SAPS E field drove the SED plume plasma poleward and sunward across the polar cap. Significantly, these scenarios show that the AAs' low precipitation-induced conductivity compensated for the sunlit conditions and thus boosted the FC-2 related eastward E field (Sandholt & Farrugia, 2006). Within these FCs (that we specified as FC-1, FC-2, and BPS arc related sunward FC), the localized earthward electromagnetic energy deposition occurring as Joule heating and particle precipitation drove localized upward drifts and upwellings (Rentz & Lühr, 2008) leading to the development of localized D_N peaks within/over these FCs. But as the strong storm-time SAPS E field drove the SED plume plasma poleward, sunward, and across the polar cap, Ne also increased within or at the edge of the polar cap. Thus, during these Scenarios 1–4, a strong I-T coupling was displayed by the simultaneously increased D_N, Ne, and Te demonstrating that Joule heating, powered by SS-FACs, fueled upwelling leading to localized increases both in D_N and in Ne (Liu et al., 2010).

As our Scenarios 5–8 demonstrate, the development of localized D_N increases continued during dayside X_H reconnection and within/over FC-4s associated with PAs and during plasmaspheric erosion events driven by the strong storm-time SAPS E fields. Significantly, we provide observational evidence that these localized D_N increases developed during FTEs and sometimes during X_H (Sc-5–Sc-6) reconnection and sometimes during simultaneous X_L–X_H reconnection under $B_Z \leq 0$ and $|B_Y|/|B_Z| \geq 1$ conditions. These D_N increases development was due to the quite intense earthward electromagnetic deposition (~170 mW/m^2 in Sc-7) within these FC-4s implying strong M-I-T coupling as the magnetosphere became preconditioned by the strong storm-time SAPS E field that swept the SED plume plasma to the ionospheric dayside cusp and magnetospheric dayside merging region (Foster et al., 2005). But the tracked low Ne (created by plasmaspheric erosion), high D_N, and mid Te might suggest a weak I-T coupling and a different underlying mechanism than upwelling fueled by Joule heating, as previous studies suggested (Liu et al., 2010). Possible suggested candidate mechanisms include the transport of neutral densities provided by large-scale travelling atmospheric disturbances (TADs) (Bruinsma & Forbes, 2007), the transport of localized upwellings from the cusp into the polar cap by the convection of SED plume plasma (Stolle et al., 2006), and the upflow of ionospheric ions generating upwellings by ion-neutral collisions (Liu et al., 2010; Pollock et al., 1990).

However, during the shock-sheath driven 7–8 November 2004 superstorm, the low Ne-high D_N was not due to a weak I-T coupling but to the action of large storm-time SAPS FCs ($V_{HOR} \approx$ 5,500 m/s) and associated SAPS E fields contributing to plasmaspheric erosion during strong M-I-T coupling. This is demonstrated with our observational results (Sc-5–Sc-8) providing evidence of plasmaspheric erosion. Furthermore, Figures 8 and 9 show also that at high latitudes, both O/N_2 and TEC started decreasing during SH3 (before t1; see Figure 9d) while NO remained minimum and both O/N_2 and TEC continued decreasing during MC1 and MC2 (between t2 and t3; see Figure 9d) while NO increased and maximized. However, the main cause of TEC decrease was not the O/N_2 decrease nor the NO increase, but the combination of strong storm-time convection and SAPS E fields, which developed during SH3 of this shock-sheath driven storm and caused plasmaspheric erosion. Adding to the relevant studies (Knipp et al., 2013, 2017; Verkhoglyadova et al., 2017), we provide observational evidence that this shock-sheath driven storm increased the asymmetry of ring current and thus led to intense SAPS FC/E field development, which—by adding to the magnetospheric convection E field—enhanced plasmaspheric erosion. The strong contrasting behavior of neural density and O/N_2 was also studied by Lei et al. (2010). Based on their model simulations produced for this storm, they show that the heat source created scale-height increase led to the significant enhancements of neutral densities and to the contrasting changes of O/N_2. Adding to their study, we provide observational evidence that this heat source occurred within FCs, during FTEs, and was fueled by the oppositely directed large-scale FACs connecting via ionospheric Pedersen currents within these FCs.

6. Conclusions

In this study, we have investigated M-I-T coupling occurring during the 7–8 November 2004 superstorm by investigating the coupling of the magnetosphere with the ionosphere and then the thermosphere. Our new findings are as follows. (1) Strong M-I-T coupling was apparent when the localized D_N increases developed within/over FCs during FTEs and near the SED plume where electron density (Ne) increases also occurred. (2) M-I-T coupling was still strong but less apparent when the localized D_N increases developed within/over FCs during FTEs and in the eroded polar cap where Ne became depleted and thus Ne increases were absent. (3) Due to plasmaspheric erosion, driven by the combination of strong convection E field and large storm-time SAPS E fields—implied by the large SAPS FCs (~3,000-5,000 m/s) detected—and not by the thermospheric composition of low O/N_2 and high NO, the high-latitude Ne and TEC became decreased poleward of the PP. The reason is that a shock-sheath driven storm, like the 7–8 November 2004 superstorm, leads to strong asymmetric ring current development—via the strong solar-wind convection E field—and thus to the development of strong storm-time SAPS E field (driving large SAPS FC), and the combination of these different E fields erode the plasmasphere.

Acknowledgments
This material is based on research sponsored by the Air Force Office of Scientific Research, under agreement number FA2386-17-1-4109. The U.S. Government is authorized to reproduce and distribute reprints for Governmental purposes notwithstanding any copyright notation thereon. We gratefully acknowledge Dr. Eelco Doornbos and the DEOS (Delft Institute for Earth Observation and Space Systems) Thermospheric web server (http://thermosphere.tudelft.nl/) for the CHAMP accelerometer data, to the GFZ German Research Centre for Geosciences for the CHAMP electron temperature data (http://isdc-old.gfz-potsdam.de/index.php?module=pagesetter&func=viewpub&tid=1&pid=34), the TIMED, LANL, Polar, and Cluster data (https://cdaweb.gsfc.nasa.gov/cdaweb/istp_public/), and the OMNI database (https://cdaweb.gsfc.nasa.gov/cdaweb/istp_public/) for the solar and magnetic data. We are thankful to Prof. Hermann Lühr for fruitful discussions and for providing the CHAMP field-aligned current estimates. Special thanks are extended to MIT for the GPS TEC data in the Madrigal Database (http://cedar.openmadrigal.org/). We are grateful to the CEDAR Archival Madrigal Database and the US Air Force for providing the DMSP thermal plasma data. We also thank the World Data Center for Geomagnetism at Kyoto (http://wdc.kugi.kyoto-u.ac.jp/wdc/Sec3.html) for providing the geomagnetic indices. Special thanks are also extended to The Johns Hopkins University Applied Physics Laboratory for the spectrogram images (http://sd-www.jhuapl.edu/Aurora/spectrogram/index.html).

References

Andalsvik, Y. L., Sandholt, P. E., & Farrugia, C. J. (2011). Dayside and nightside contributions to cross-polar cap potential variations: The 20 March 2001 ICME case. *Annales Geophysicae*, *29*(11), 2189–2201. https://doi.org/10.5194/angeo-29-2189-2011

Anderson, P. C., Carpenter, D. L., Tsuruda, K., Mukai, T., & Rich, F. J. (2001). Multisatellite observations of rapid subauroral ion drifts (SAID). *Journal of Geophysical Research*, *106*(A12), 29,585–29,599. https://doi.org/10.1029/2001JA000128

Anderson, P. C., Hanson, W. B., Heelis, R. A., Craven, J. D., Baker, D. N., & Frank, L. A. (1993). A proposed production-model of rapid subauroral ion drifts and their relationship to substorm evolution. *Journal of Geophysical Research*, *98*(A4), 6069–6078. https://doi.org/10.1029/92JA01975

Balogh, A., Carr, C. M., Acuña, M. H., Dunlop, M. W., Beek, T. J., Brown, P., et al. (2001). The Cluster magnetic field investigation: Overview of in-flight performance and initial results. *Annales Geophysicae*, *19*(10/12), 1207–1217. https://doi.org/10.5194/angeo-19-1207-2001

Birn, J., Thomsen, M. F., Borovsky, J. E., Reeves, G. D., McComas, D. J., Belian, R. D., & Hesse, M. (1998). Substorm electron injections: Geosynchronous observations and test particle simulations. *Journal of Geophysical Research*, *103*(A5), 9235–9248. https://doi.org/10.1029/97JA02635

Bruinsma, S. L. & Forbes, J. M. (2007). Global observation of traveling atmospheric disturbances (TADs) in the thermosphere. *Geophysical Research Letters*, *34*(14), L14103. https://doi.org/10.1029/2007GL030243

Carlson, H. C., Spain, T., Aruliah, A., Skjaeveland, A., & Moen, J. (2012). First-principles physics of cusp/polar cap thermospheric disturbances. *Geophysical Research Letters*, *39*, L19103. https://doi.org/10.1029/2012GL053034

Clilverd, M. A., Jenkins, B., & Thomson, N. R. (2000). Plasmaspheric storm time erosion. *Journal of Geophysical Research*, *105*(A6), 12,997–13,008. https://doi.org/10.1029/1999JA900497

Coster, A. J., Colerico, M. J., Foster, J. C., Rideout, W., & Rich, F. (2007). Longitude sector comparisons of storm enhanced density. *Geophysical Research Letters*, *34*, L18105. https://doi.org/10.1029/2007GL030682

Doornbos, E., van den Ijssel, J., Lühr, H., Forster, M., & Koppenwallner, G. (2010). Neutral density and crosswind determination from arbitrarily oriented multi-axis accelerometers on satellites. *Journal of Spacecraft and Rockets*, *47*(4), 580–589. https://doi.org/10.2514/1.48114

Du, A. M., Tsurutani, B. T., & Sun, W. (2008). Anomalous geomagnetic storm of 21–22 January 2005: A storm main phase during northward IMFs. *Journal of Geophysical Research*, *113*, A10214. https://doi.org/10.1029/2008JA013284

Dungey, J. (1963). The structure of the exosphere or adventures in velocity space. In C. DeWitt, J. Hieblot, & A. Lebeau (Eds.), *Geophysics, The Earth's Environment*, (pp. 505–550). New York: Gordon & Breach.

Dungey, J. W. (1961). Interplanetary magnetic field and the auroral zones. *Physical Review Letters*, *6*(2), 47–48. https://doi.org/10.1103/PhysRevLett.6.47

Echer, E., Tsurutani, B. T., & Guarnieri, F. L. (2009). Solar and interplanetary origins of the November 2004 superstorms. *Advances in Space Research*, *44*(5), 615–620. https://doi.org/10.1016/j.asr.2009.05.003

Echer, E., Tsurutani, B. T., & Guarnieri, F. L. (2010). Interplanetary origins of November 2004 superstorms. *Journal of Atmospheric and Solar-Terrestrial Physics*, *72*(4), 280–284. https://doi.org/10.1016/j.jastp.2009.02.009

Farrugia, C. J., Sandholt, P. E., Maynard, N. C., Torbert, R. B., & Ober, D. M. (2003). Temporal variations in a four-sheet field-aligned current system and associated aurorae as observed during a Polar-ground magnetic conjunction in the midmorning sector. *Journal of Geophysical Research*, *108*(A6), 1230. https://doi.org/10.1029/2002JA009619

Fejer, B. G., Jensen, J. W., Kikuchi, T., Abdu, M. A., & Chau, J. L. (2007). Equatorial ionospheric electric fields during the November 2004 magnetic storm. *Journal of Geophysical Research*, *112*, A10304. https://doi.org/10.1029/2007JA012376

Foster, J. C. (1993). Storm time plasma transport at middle and high latitudes. *Journal of Geophysical Research*, *98*(A2), 1675–1689. https://doi.org/10.1029/92JA02032

Foster, J. C., & Burke, W. J. (2002). SAPS: A new characterization for sub-auroral electric fields. *Eos, Transactions American Geophysical Union*, *83*, 393–394. https://doi.org/10.1029/2002EO000289

Foster, J. C., Coster, A. J., Erickson, P. J., Holt, J. M., Lind, F. D., Rideout, W., et al. (2005). Multiradar observations of the polar tongue of ionization. *Journal of Geophysical Research*, *110*, A09S31. https://doi.org/10.1029/2004JA010928

Foster, J. C., Coster, A. J., Erickson, P. J., Rich, F. J., & Sandel, B. R. (2004). Stormtime observations of the flux of plasmaspheric ions to the dayside cusp/magnetopause. *Geophysical Research Letters*, *31*, L08809. https://doi.org/10.1029/2004GL020082

Foster, J. C., Erickson, P. J., Coster, A. J., Goldstein, J., & Rich, F. J. (2002). Ionospheric signatures of plasmaspheric tails. *Geophysical Research Letters*, *29*(13), 1623. https://doi.org/10.1029/2002GL015067

Foster, J. C., Rideout, W., Sandel, B., Forrester, W. T., & Rich, F. J. (2007). On the relationship of SAPS to storm-enhanced density. *Journal of Atmospheric and Solar-Terrestrial Physics*, *69*, 303–313. https://doi.org/10.1016/j.jastp.2006.07.021

Glassmeier, K.-H., & Stellmacher, M. (1996). Mapping of flux transfer events to the ionosphere. *Advances in Space Research*, *18*(8), 151–160. https://doi.org/10.1016/0273-1177(95)00983-3

Goldstein, J., Sandel, B. R., Thomsen, M. F., Spasojevic, M., & Reiff, P. H. (2004). Simultaneous remote sensing and in situ observations of plasmaspheric drainage plumes. *Journal of Geophysical Research*, *109*, A03202. https://doi.org/10.1029/2003JA010281

Goldstein, J., Spasojević, M., Reiff, P. H., Sandel, B. R., Forrester, W. T., Gallagher, D. L., & Reinisch, B. W. (2003). Identifying the plasmapause in IMAGE EUV data using IMAGE RPI in situ steep density gradients. *Journal of Geophysical Research*, *108*(A4), 1147. https://doi.org/10.1029/2002JA009475

Grebowsky, J. M. (1970). Model study of plasmapause motion. *Journal of Geophysical Research*, *75*, 4329–4333. https://doi.org/10.1029/JA075i022p04329

Harvey, P., Mozer, F. S., Pankow, D., Wygant, J., Maynard, N. C., Singer, H., et al. (1995). The electric field instrument on the polar satellite. *Space Science Reviews*, *71*(1-4), 583–596. https://doi.org/10.1007/BF00751342

Huang, C. Y., & Burke, W. J. (2004). Transient sheets of field-aligned current observed by DMSP during the main phase of a magnetic superstorm. *Journal of Geophysical Research*, *109*, A06303. https://doi.org/10.1029/2003JA010067

Huang, C. Y., Su, Y.-J., Sutton, E. K., Weimer, D. R., & Davidson, R. L. (2014). Energy coupling during the August 2011 magnetic storm. *Journal of Geophysical Research: Space Physics*, *119*, 1219–1232. https://doi.org/10.1002/2013JA019297

Iijima, T., & Potemra, T. A. (1978). Large-scale characteristics of field aligned currents associated with substorms. *Journal of Geophysical Research*, *83*(A2), 599–615. https://doi.org/10.1029/JA083iA02p00599

Kil, H., Kwak, Y.-S., Paxton, L. J., Meier, R. R., & Zhang, Y. (2011). O and N2 disturbances in the F region during the 20 November 2003 storm seen from TIMED/GUVI. *Journal of Geophysical Research*, *116*, A02314. https://doi.org/10.1029/2010JA016227

Kim, K.-H., Goldstein, J., & Berube, D. (2007). Plasmaspheric drainage plume observed by the Polar satellite in the prenoon sector and the IMAGE satellite during the magnetic storm of 11 April 2001. *Journal of Geophysical Research*, *112*, A06237. https://doi.org/10.1029/2006JA012030

Knipp, D., Eriksson, S., Kilcommons, L., Crowley, G., Lei, J., Hairston, M., & Drake, K. (2011). Extreme Poynting flux in the dayside thermosphere: Examples and statistics. *Geophysical Research Letters*, *38*, L16102. https://doi.org/10.1029/2011GL048302

Knipp, D., Kilcommons, L., Hunt, L., Mlynczak, M., Pilipenko, V., Bowman, B., et al. (2013). Thermospheric damping response to sheath-enhanced geospace storms. *Geophysical Research Letters*, *40*, 1263–1267. https://doi.org/10.1002/grl.50197

Knipp, D. J., Pette, D. V., Kilcommons, L. M., Isaacs, T. L., Cruz, A. A., Mlynczak, M. G., et al. (2017). Thermospheric nitric oxide response to shock-led storms. *Space Weather*, *15*, 325–342. https://doi.org/10.1002/2016SW001567

Kuo, H., Russell, C. T., & Le, G. (1995). Statistical studies of flux transfer events. *Journal of Geophysical Research*, *100*, 3513–3519. https://doi.org/10.1029/94JA02498

Le, G., Zheng, Y., Russell, C. T., Pfaff, R. F., Slavin, J. A., Lin, N., et al. (2008). Flux transfer events simultaneously observed by Polar and Cluster: Flux rope in the subsolar region and flux tube addition to the polar cusp. *Journal of Geophysical Research*, *113*, A01205. https://doi.org/10.1029/2007JA012377

Lei, J., Thayer, J. P., Burns, A. G., Lu, G., & Deng, Y. (2010). Wind and temperature effects on thermosphere mass density response to the November 2004 geomagnetic storm. *Journal of Geophysical Research*, *115*, A05303. https://doi.org/10.1029/2009JA014754

Liu, R., Lühr, H., & Ma, S.-Y. (2010). Storm-time related mass density anomalies in the polar cap as observed by CHAMP. *Annales Geophysicae*, *28*, 165–180. https://doi.org/10.5194/angeo-28-165-2010

Lühr, H., Rother, M., Kähler, W., Ritter, P., & Grunwaldt, L. (2004). Thermospheric up-welling in the cusp region: Evidence from CHAMP observations. *Geophysical Research Letters*, *31*, L06805. https://doi.org/10.1029/2003GL019314

Marklund, G. (1984) Auroral arc classification scheme based on the observed arc-associated electric field pattern. *Planetary and Space Science*, *32*(2),193–211. https://doi.org/10.1016/0032-0633(84)90154-5

Mishin, E. (2013). Interaction of substorm injections with the subauroral Geospace: 1. Multispacecraft observations of SAID. *Journal of Geophysical Research: Space Physics*, *118*, 5782–5796. https://doi.org/10.1002/jgra.50548

Mishin, E. V., Burke, W. J., Huang, C. Y., & Rich, F. J. (2003). Electromagnetic wave structures within subauroral polarization streams. *Journal of Geophysical Research*, *108*(A8), 1309. https://doi.org/10.1029/2002JA009793

Neudegg, D. A., Cowley, S. W. H., Milan, S. E., Yeoman, T. K., Lester, M., Provan, G., et al. (2000). A survey of magnetopause FTEs and associated flow bursts in the polar ionosphere. *Annales Geophysicae*, *18*(4), 416–435. https://doi.org/10.1007/s00585-000-0416-0

Pitout, F., Bosqued, J.-M., Alcaydé, D., Denig, W. F., & Rème, H. (2001). Observations of the cusp region under northward IMF. *Annales Geophysicae*, *19*, 1641–1653. https://doi.org/10.5194/angeo-19-1641-2001

Pollock, C. J., Chandler, M. O., Moore, T. E., Waite, J. H. Jr., Chappell, C. R., & Gurnett, D. A. (1990). A survey of upwelling ion event characteristics. *Journal of Geophysical Research*, *95*(A11), 18,969–18,980. https://doi.org/10.1029/JA095iA11p18969

Prolss, G. W. (2006). Electron temperature enhancement beneath the magnetospheric cusp. *Journal of Geophysical Research*, *111*, A07304. https://doi.org/10.1029/2006JA011618

Puhl-Quinn, P. A., Matsui, H., Mishin, E., Mouikis, C., Kistler, L., Khotyaintsev, Y., Décréau, P. M. E., & Lucek, E. (2007). Cluster and DMSP observations of SAID electric fields. *Journal of Geophysical Research*, *112*(A5), A05219. https://doi.org/10.1029/2006JA012065

Rème, H., Aoustin, C., Bosqued, J. M., Dandouras, I., Lavraud, B., Sauvaud, J. A., et al. (2001). First multispacecraft ion measurements in and near the Earth's magnetosphere with the identical Cluster ion spectrometry (CIS) experiment. *Annales Geophysicae*, *19*(10/12), 1303–1354. https://doi.org/10.5194/angeo-19-1303-2001

Rentz, S., & Lühr, H. (2008). Climatology of the cusp-related thermospheric mass density anomaly, as derived from CHAMP observations. *Annales de Geophysique*, *26*(9), 2807–2823. https://doi.org/10.5194/angeo-26-2807-2008

Rijnbeek, R. P., Cowley, S. W. H., Southwood, D. J., & Russell, C. T. (1984). A survey of dayside flux transfer events observed by ISEE 1 and 2 magnetometers. *Journal of Geophysical Research*, *89*(A2), 786–800. https://doi.org/10.1029/JA089iA02p00786

Rishbeth, H. (1998). How the thermospheric circulation affects the ionospheric F2 layer. *Journal of Atmospheric and Solar-Terrestrial Physics*, *60*, 1385–1402. https://doi.org/10.1016/S1364-6826(98)00062-5

Russell, C. T., & Elphic, R. C. (1978). Initial ISEE magnetometer results: Magnetopause observations. *Space Science Reviews*, *22*(6), 681–715. https://doi.org/10.1007/BF00212619

Russell, C. T., & Elphic, R. C. (1979). ISEE observations of flux transfer events at the dayside magnetopause. *Geophysical Research Letters*, *6*(1), 33–36. https://doi.org/10.1029/GL006i001p00033

Russell, C. T., Le, G., & Kuo, H. (1996). The occurrence rate of flux transfer events. *Advances in Space Research*, *18*(8), 197–205. https://doi.org/10.1016/0273-1177(95)00965-5

Russell III, J. M., Mlynczak, M. G., Gordley, L. L., Tansock, J., & Esplin, R. (1999). An overview of the SABER experiment and preliminary calibration results. Proceedings of the SPIE, 44th Annual Meeting, Denver, Colorado, 18–23 July 1999, 3756, 277–288

Sadler, F. B., Lessard, M., Lund, E., Otto, A., & Lühr, H. (2012). Auroral precipitation/ion upwelling as a driver of neutral density enhancement in the cusp. *Journal of Atmospheric and Solar-Terrestrial Physics*, *87–88*, 82–90. https://doi.org/10.1016/j.jastp.2012.03.003

Sandholt, P. E., Andalsvik, Y., & Farrugia, C. J. (2010). Polar cap flow channel events: Spontaneous and driven responses. *Annales Geophysicae*, *28*, 2015–2025. https://doi.org/10.5194/angeo-28-2015-2010

Sandholt, P. E., Egeland, A., Lybekk, B., Deehr, C. S., Sivjee, G. G., & Romick, G. J. (1983). Effects of interplanetary magnetic field and magnetospheric substorm variations on the dayside aurora. *Planetary and Space Science*, *31*(11), 1345–1362. https://doi.org/10.1016/0032-0633(83)90071-5

Sandholt, P. E., & Farrugia, C. J. (2002). Monitoring magnetosheath-magnetosphere interconnection topology from the aurora. *Annales Geophysicae*, *20*, 629–637. https://doi.org/10.5194/angeo-20-629-2002

Sandholt, P. E., & Farrugia, C. J. (2006). Spatiotemporal structure of the reconnecting magnetosphere under By-dominated interplanetary magnetic cloud conditions. *Journal of Geophysical Research*, *111*, A10209. https://doi.org/10.1029/2005JA011514

Sandholt, P. E., & Farrugia, C. J. (2009). Plasma flow channels at the dawn/dusk polar cap boundaries: Momentum transfer on old open field lines and the roles of IMF By and conductivity gradients. *Annales Geophysicae*, *27*, 1527–1554. https://doi.org/10.5194/angeo-27-1527-2009

Sandholt, P. E., & Farrugia, C. J. (2012). Plasma flows, Birkeland currents and auroral forms in relation to the Svalgaard-Mansurov effect. *Annales Geophysicae*, *30*, 817–830. https://doi.org/10.5194/angeo-30-817-2012

Sandholt, P. E., Farrugia, C. J., & Denig, W. F. (2004). Detailed dayside auroral morphology as a function of local time for southeast IMF orientation: Implications for solar wind-magnetosphere coupling. *Annales Geophysicae*, *22*, 3537–3560. https://doi.org/10.5194/angeo-22-3537-2004

Sandholt, P. E., Farrugia, C. J., Øieroset, M., Stauning, P., & Cowley, S. W. H. (1996). Auroral signature of lobe reconnection. *Journal of Geophysical Research*, *23*(14), 1725–1728. https://doi.org/10.1029/96GL01846

Sandholt, P. E., Lockwood, M., Oguti, T., Cowley, S. W. H., Freeman, K. S. C., Lybekk, B., Egeland, A. & Willis, D. M. (1990). Midday auroral breakup events and related energy and momentum transfer from the magnetosheath. *Journal of Geophysical Research*, *95*(A2), 1039–1060. https://doi.org/10.1029/JA095iA02p01039

Sandholt, P. E., & Newell, P. T. (1992). Ground and satellite observations of an auroral event at the cusp/cleft equatorward boundary. *Journal of Geophysical Research*, *97*(A6), 8685–8691. https://doi.org/10.1029/91JA02995

Scudder, J., Hunsacker, F., Miller, G., Lobell, J., Zawistowski, T., Ogilvie, K., et al. (1995). Hydra—A 3-dimensional electron and ion hot plasma instrument for the Polar spacecraft of the GGS mission. *Space Science Reviews*, *71*(1-4), 459–495. https://doi.org/10.1007/BF00751338

Southwood, D. J. (1987). The ionospheric signature of flux transfer events. *Journal of Geophysical Research*, *92*(A41), 3207–3213. https://doi.org/10.1029/JA092iA04p03207

Southwood, D. J., & Wolf, R. A. (1978). An assessment of the role of precipitation in magnetospheric convection. *Journal of Geophysical Research*, *83*(A11), 5227–5232. https://doi.org/10.1029/JA083iA11p05227

Stolle, C., Lilensten, J., Schlüter, S., Jacobi, C., Rietveld, M., & Lühr, H. (2006). Observing the north polar ionosphere on 30 October 2003 by GPS imaging and IS radars. *Annales Geophysicae*, *24*, 107–113. https://doi.org/10.5194/angeo-24-107-2006

Titheridge, J. E. (1976). Plasmapause effects in the top side ionosphere. *Journal of Geophysical Research*, *81*(19), 3227–3233. https://doi.org/10.1029/JA081i019p03227

Tsurutani, B., Mannucci, A., Iijima, B., Abdu, M. A., Sobral, J. H. A., Gonzalez, W., et al. (2004). Global dayside ionospheric uplift and enhancement associated with interplanetary electric fields. *Journal of Geophysical Research*, *109*, A08302. https://doi.org/10.1029/2003JA010342

Tsurutani, B. T., Echer, E., Guarnieri, F. L., & Kozyra, J. U. (2008). CAWSES November 7–8, 2004, superstorm: Complex solar and interplanetary features in the post-solar maximum phase. *Geophysical Research Letters*, *35*, L06S05. https://doi.org/10.1029/2007GL031473

Tsurutani, B. T., Gonzalez, W. D., Tang, F., Akasofu, S. I., & Smith, E. J. (1988). Origin of interplanetary southward magnetic fields responsible for major magnetic storms near solar maximum (1978–1979). *Journal of Geophysical Research*, *93*(A8), 8519–8531. https://doi.org/10.1029/JA093iA08p08519

Verkhoglyadova, O. P., Komjathy, A., Mannucci, A. J., Mlynczak, M. G., Hunt, L. A., & Paxton, L. J. (2017). Revisiting ionosphere-thermosphere responses to solar wind driving in superstorms of November 2003 and 2004. *Journal of Geophysical Research: Space Physics*, *122*, 10,824–10,850. https://doi.org/10.1002/2017JA024542

Vlasov, M., Kelley, M. C., & Kil, H. (2003). Analysis of ground-based and satellite observations of F region behavior during the great magnetic storm of July 15, 2000. *Journal of Atmospheric and Solar-Terrestrial Physics*, *65*, 1223–1234. https://doi.org/10.1016/j.jastp.2003.08.012